Clim. Past Discuss., 9, 3239–3306, 2013
www.clim-past-discuss.net/9/3239/2013/
doi:10.5194/cpd-9-3239-2013

Climate of the Past
Discussions
Open Access

Discussion Paper | Discussion Paper | Discussion Paper | Discussion Paper |

Assessing the impact of Laurentide Ice-Sheet topography on glacial climate

D. J. Ullman[1], A. N. LeGrande[2], A. E. Carlson[1,3], F. S. Anslow[4], and J. M. Licciardi[5]

[1]Department of Geoscience, University of Wisconsin-Madison, Madison, WI, USA
[2]NASA Goddard Institute for Space Studies and Columbia University, New York, NY, USA
[3]College of Earth, Ocean, and Atmospheric Sciences, Oregon State University, Corvallis, OR, USA
[4]Pacific Climate Impact Consortium, University of Victoria, Victoria, BC, Canada
[5]Department of Earth Sciences, University of New Hampshire, Durham, NH, USA

Received: 10 May 2013 – Accepted: 4 June 2013 – Published: 18 June 2013

Correspondence to: D. J. Ullman (ullman@wisc.edu)

Published by Copernicus Publications on behalf of the European Geosciences Union.

Abstract

Simulations of past climates require altered boundary conditions to account for known shifts in the Earth system. For the Last Glacial Maximum (LGM) and subsequent deglaciation, the existence of large Northern Hemisphere ice sheets provides a profound change in surface topography and albedo. While ice-sheet extent is fairly well known, numerous conflicting reconstructions of ice-sheet topography suggest that precision in this boundary condition is lacking. Here we use a high-resolution and oxygen-isotope-enabled fully-coupled global circulation model (GCM) (GISS ModelE2-R), along with two different reconstructions of the Laurentide Ice Sheet (LIS) that provide maximum and minimum estimates of LIS elevation, to assess the range of climate variability in response to uncertainty in this boundary condition. We present this comparison at two equilibrium time slices: the LGM, where differences in ice sheet topography are maximized, and 14 ka, where differences in maximum ice sheet height are smaller but still exist. Overall, we find significant differences in the climate response to LIS topography, with the larger LIS resulting in enhanced Atlantic meridional overturning circulation and warmer surface air temperatures, particularly over Northeast Asia and the North Pacific. These up and downstream effects are associated with differences in the development of planetary waves in the upper atmosphere, with the larger LIS resulting in a weaker trough over Northeast Asia that leads to the warmer temperatures and decreased albedo from snow and sea-ice cover. Differences between the 14 ka simulations are similar in spatial extent but smaller in magnitude, suggesting that climate is responding primarily to the larger difference in maximum LIS elevation in the LGM simulations. These results suggest that such uncertainty in ice-sheet boundary conditions alone may greatly impact the results of paleoclimate simulations and their ability to successfully simulate past climates, with implications for estimating climate sensitivity to greenhouse gas forcing utilizing past climate states.

1 Introduction

The Last Glacial Maximum (LGM; ~ 21 ka) provides a valuable target to test the ability of general circulation models (GCMs) to simulate a climate for which they were not designed (Mix et al., 2001; IPCC AR4 WG1, 2007; Bracconot et al., 2012) and is a possible means of assessing climate sensitivity to changes in atmospheric CO_2 (Crucifix, 2006; Hansen et al., 2008; Schmittner et al., 2011, 2012; Fyke and Eby, 2012; Hargreaves et al., 2012; PALAEOSENS, 2012). The last deglaciation (~ 20 to 7 ka) was the most recent period when changes in Earth's orbit around the Sun caused Northern Hemisphere ice-sheet retreat (Clark et al., 2009; Carlson and Winsor, 2012; He et al., 2013) and rising atmospheric greenhouse gas concentration (Monnin et al., 2001; Lemieux-Dudon et al., 2010), which provides an evolving climate state (Shakun and Carlson, 2010) for testing GCMs (e.g., Timm and Timmerman, 2007; Liu et al., 2009; Shakun et al., 2012; Gregoire et al., 2012; He et al., 2013). For instance, by 14 ka, Northern Hemisphere ice sheets were still relatively large (60–70 % remaining by area; Dyke, 2004; Gyllencreutz et al., 2007), but atmospheric greenhouse gas concentrations had already risen by ~ 60 % of their total deglacial change (Monnin et al., 2001; Lemieux-Dudon et al., 2010) and boreal summer insolation was ~ 7.5 % higher than present/LGM levels (Berger and Loutre, 1991).

However, the simulated glacial state in any one model is sensitive to the boundary conditions used as a starting point for the simulation (Manabe and Broccoli, 1985; Broccoli and Manabe, 1987; Hyde and Peltier, 1993; Abe-Ouchi et al., 2007; Liu et al., 2009; Pausata et al., 2011; Hofer et al., 2012). Thus, uncertainty in a particular set of glacial boundary conditions may overshadow a GCM's simulated change in climate and its ability to constrain climate sensitivity using the LGM as a starting point. Along this line, Hargreaves et al. (2012) suggested that disregarding high latitude response at the LGM which avoids bringing this ambiguity into climate sensitivity work, although this then ignores many climate feedbacks. Some of the important boundary conditions are well documented, such as the orbital parameters that drive the magnitude and seasonality of insolation (Berger and Loutre, 1991), and the concentration of atmospheric greenhouse gases (Monnin et al., 2004; Jouzel et al., 2007; Lüthi et al., 2008; Lemieux-Dudon et al., 2010). Other boundary conditions of past glacial climates have proven to be more elusive. The aerosol forcing (particularly dust and black carbon) at the LGM and through the deglaciation is known only at individual locations, with limited spatial resolution (Petit et al., 1981; Thompson et al., 1995; Mahowald et al., 1999; Reader et al., 1999; Power et al., 2008). While large uncertainties still remain on the impact of aerosols on radiative forcing (Penner et al., 2004; Lohmann and Feichter, 2005; Forster et al., 2007; Chylek and Lohmann, 2008), the LGM dust loading may issue a forcing on the order of $\sim -1\,\mathrm{W\,m^{-2}}$ that is comparable to changes in greenhouse gases alone ($\sim -2.85\,\mathrm{W\,m^{-2}}$), at least in the tropics, where ice sheet albedo is not a factor (Harrison et al., 2001; Claquin et al., 2003; Crucifix, 2006). Likewise, reconstructions of LGM and deglacial vegetation and the related impact on surface albedo are limited to low resolution global approximations and higher resolution estimates that are only regional in scope (Jackson et al., 2000; Prentice et al., 2000; Harrison et al., 2001; Ray and Adams, 2001; Bigelow et al., 2003; Williams, 2003; Pickett et al., 2004; Williams et al., 2011).

Perhaps the greatest source of uncertainty in glacial boundary conditions relates to ice-sheet thickness. Although the geographical extent of LGM and deglacial ice-sheet extents are fairly well mapped (Denton and Hughes, 1981, 2002; Dyke and Prest, 1987; Anderson et al., 2002; Clark and Mix, 2002; Bennike and Björck, 2002; Dyke, 2004; Gyllencreutz et al., 2007), direct observations of ice thickness and topography are limited and usually absent for the highest/thickest portions of the ice sheets (e.g., Denton and Hughes, 1981, 2002; Dyke et al., 2002; Clark et al., 1992, 2009; Goehring et al., 2008; Carlson and Clark, 2012). Therefore, ice-sheet height must be simulated through geophysical or glaciological modeling approaches. The reconstructions of ICE-4G, ICE-5G, and ICE-6G (Peltier, 1994, 2004; Toscano et al., 2011) have proven to be useful ice-sheet boundary conditions to employ in GCMs due to their geophysically-based solutions, global scope, and product availability. However, the differences between these

CPD
9, 3239–3306, 2013

reconstructions (Peltier, 2004; Toscano et al., 2011), as well as other ice-sheet-specific reconstructions (Clark et al., 1996; Licciardi et al., 1998; Tarasov and Peltier, 2004; Argus and Peltier, 2010; Lambeck et al., 2010) suggest that there is a large range in existing ice-sheet boundary conditions, particularly for the Laurentide Ice Sheet (LIS).

This large uncertainty between reconstructions of ice-sheet geometry is unfortunate considering that glacial topography is one of the dominant drivers of atmospheric and oceanic circulation, temperature, and precipitation in simulations of deglacial climate (Abe-Ouchi et al., 2007; Pausata et al., 2011; Hofer et al., 2012; Tharammal et al., 2012). Glacial orography leads to reduced surface air temperatures through vertical lapse rate alone, but the presence of these large ice mountains also has been shown to have downstream effects, altering upper atmosphere flow (Cook and Held, 1988; Bromwich et al., 2004; Abe-Ouchi et al., 2007; Langen and Vinther, 2009), midlatitude storm tracks and wintertime precipitation (Kageyama et al., 1999; Hofer et al., 2012), and Atlantic meridional overturning circulation (AMOC) strength (Yu et al., 1996; Adkins et al., 2002; Wunsch, 2003; Curry and Oppo, 2005; Lynch-Steiglitz et al., 2007; Otto-Bliesner et al., 2007; Weber et al., 2007; Arzel et al., 2008).

Here we test the impact that LIS geometry had on LGM and deglacial climate using two alternate reconstructions of LIS topography that provide upper and lower bounds for this boundary condition. As an upper bound, we use ICE-5G (VM2) (Peltier, 2004; hereafter 5G), which has the highest LIS topography of any LIS reconstruction, with a dominant ice dome over the western Keewatin sector (Fig. 1). As a lower bound, we employ the dynamics-driven flow-line reconstruction of Licciardi et al. (1998; hereafter L) (Fig. 1). The maximum height of this reconstruction is comparable to ICE-4G (Peltier et al., 1994; Clark et al., 1996), but it is ~ 20 % lower than that of ICE-5G, particularly over the western LIS (Fig. 1). The use of these reconstructions is a particularly relevant assessment of the range of variability in the Paleoclimate Modeling Intercomparison Project 3 (PMIP3) topographic boundary conditions, as the maximum ice-sheet heights of the 3 ice sheet reconstructions used to create the averaged topography of the LIS in the PMIP3 (http://pmip3.lsce.ipsl.fr/) lie in between the upper and lower bounds used in

CPD
9, 3239–3306, 2013

our study. We compare the effects of these LIS boundary conditions at two time periods, 21 and 14 ka, to assess the impact of varying LIS topography under different climate forcing conditions. The 21 ka simulations provide a test of topographic variability under full LGM boundary conditions with different LIS maximum elevations. At 14 ka, both LIS topographies are reduced and differences between maximum LIS elevation are smaller (∼ 15 %). The 14 ka simulations provide a test of ice sheet geometry differences under a different forcing scenario, with changes in precession, obliquity, and increased atmospheric greenhouse gas concentrations.

2 Methods

2.1 Model

The NASA Goddard Institute for Space Studies (GISS) ModelE2, coupled to the Russell (Russel et al., 2000) ocean is a fully-coupled atmospheric-ocean global climate model (Schmidt et al., 2013). We use the same version of ModelE2-R as is being used for the Coupled Model Intercomparison Project Phase 5 (CMIP5) simulations (NINT physics version), with an atmosphere resolution of 2° latitude by 2.5° longitude with 40 vertical layers up to 0.1 mb, and an ocean resolution of 1° latitude by 1.25° longitude with 32 depth layers. ModelE2-R includes passive water isotopologue tracers (i.e., $H_2^{18}O$, HDO, here after referred to as water isotopes), removing one degree of uncertainty when comparing its diagnostics to paleoclimate reconstructions based on water isotope variability (e.g., ice cores, speleothems, ocean foraminifera) to test model skill (e.g., LeGrande et al., 2006; Carlson et al., 2008a,b; LeGrande and Schmidt, 2009).

2.2 Boundary conditions

Each simulation uses appropriate insolation for the time period owing to changes in orbital parameters (Berger and Loutre, 1991), along with appropriate glacial greenhouse gas concentrations (Joos and Spahni, 2008) (Table 1). Coastline and basin geometry

CPD
9, 3239–3306, 2013

were adjusted to reflect an ∼ 120 m lowering in sea level at 21 ka and a ∼ 86 m lowering at 14 ka, in accordance with the volume of water contained in ice sheet boundary conditions (Peltier, 2004). The volume of water held in the two alternate LIS reconstructions is different. However, to minimize the differences between our simulations, we kept the ocean bathymetry (and the land/sea mask) the same. The ModelE2-R ocean uses straits – essentially pipelines for ocean tracers and mass – in the modern to accommodate sub grid scale passages. All straits were eliminated (because of sea level lowering) except for Gibraltar and Bab Al Mandab, and no new straits were created.

ModelE2 does not have a dynamic vegetation component, and so terrestrial vegetation cover was assigned according to mapped conditions at the LGM (25 000–15 000 yr BP; Ray and Adams, 2001) for regions not covered by ice sheets. A separate reconstruction for 14 ka does not exist, therefore we continued to use this LGM reconstruction, modified slightly to account for changes in ice sheet extend by expanding nearby vegetation types into these areas no longer covered by ice. Continental river routing was assigned in accordance with ice-sheet configuration and its impact on drainage basins (e.g., Licciardi et al., 1998, 1999; Peltier, 2004).

2.3 Ice-sheet geometry sensitivity

To test the influence of ice sheet topography on glacial climate and surface mass balance, two separate simulations were conducted at each time slice using two alternate reconstructions of LIS topography: one using the geophysically-based ICE-5G (5G; Peltier, 2004), and the other using the same extent of ICE-5G but replacing the LIS sector topography with that of an alternate reconstruction based on a flow-line model that simulates glacier dynamics over deformable and rigid beds with varying till viscosities (L; Licciardi et al., 1998). We use the maximum reconstructions from Licciardi et al. (1998) that incorporate higher specified effective till viscosities. In both simulations, all other ice sheet topographies and extents (Greenland, Scandinavian, etc.) are assigned using ICE-5G. We focus on the LIS because it was the largest of the Quater-

CPD
9, 3239–3306, 2013

nary ice sheets with presumably the greatest effect on climate (Alley and Clark, 1999; Clark et al., 1999; Clark and Mix, 2002; Carlson and Clark, 2012).

The two LIS reconstructions have significantly different topographies (Fig. 1). At 21 ka, the 5G-reconstruction provides a much taller LIS, particularly the Keewatin Dome over western Canada, with elevations across this region at or above 4000 m. The 21 ka L-reconstruction is lower in maximum height and moves more of the ice mass to the east with 3 distinct ice domes centered over Keewatin, southern Ontario, and central Quebec. Comparatively, the 5G-LIS has a lower topography over eastern Ontario and Quebec, but the large Keewatin dome dominates the western topography. Additionally, the 5G-reconstruction has more abrupt changes in topography whereas the L-reconstruction has smoother transitions from high to low elevations, as would be expected from a flow line model of ice deformation over hard and soft beds and similar to inferences from the geologic record (Dyke and Prest, 1987; Jenson et al., 1996).

At 14 ka, both reconstructions retain the same general geometry as 21 ka, but absolute topography is diminished (Fig. 1). ICE-5G still has a dominant Keewatin dome, while the L-reconstruction continues to have 3 prominent domes. The L-reconstruction exhibits only a small diminution in ice topography over the Ontario and Quebec domes, such that a west-east dipole in topography difference exists between the two reconstructions (Fig. 1).

Our climate model simulations were started before the PMIP3 protocol for LGM conditions had been determined, but our selection of LIS boundary conditions provide limits of topographic uncertainty that go into the PMIP3 LIS elevations. The LIS in the PMIP3 boundary conditions is similar in geometry to ICE-5G (with higher Keewatin dome over western Canada and lower topography over eastern Ontario and Quebec), but the maximum topography of the LIS in PMIP3 is more similar to the LIS reconstruction used in 21 ka-L (Fig. 1).

2.4 Equilibrium simulations – 21 ka, 14 ka, 0 ka

A control simulation (0 ka) with water isotopes was initiated from a 700 yearlong spin up from Levitus and Boyer (1994a,b) and Levitus et al. (1994), and run an additional 1000 yr. The 21 ka and 14 ka simulations were also initiated from the same 700 year-long spin up from Levitus and Boyer (1994a,b) and Levitus et al. (1994), but these experiments have altered mean ocean δ^{18}O, δD, and salinity (see section below), the last of which required a much longer integration of 1500 yr for the ocean density structure to adjust. Surface air temperature (SAT) drift is significant for the first 500 yr in each of the deglacial/glacial simulations – some of which is related to a temporary enhancement of AMOC due to the method with which enhanced salinity was applied (fractional increases were added to each grid box, where in reality additional salinity would have likely been preferentially buried in the deep ocean). After 1500 yr of integration, SAT drift is less than 0.03 °C per century, surface ocean temperature drift less than 0.02 °C per century, and deep ocean temperature drift less than 0.03 °C per century and in each of the simulations, but overall drift is never absent. Note that these simulations run 500 yr longer than those present in the Coupled Model Intercomparison Project Phase 5 (CMIP5) archive to insure that the water isotopologues have come into equilibrium (water isotopes are not a part of the CMIP5 archive). Initially, each simulation had an enhanced ocean circulation, which diminished with approach toward equilibrium. Additionally, cold surface temperatures drove sea ice growth requiring an expansion of the land mask. Here we present the final 100 yr of this simulation.

2.5 Water isotopes

ModelE2-R includes water isotopologue tracers that allow for the direct comparison of δ^{18}O measurements taken from ice cores, speleothems, ocean sediments, and other paleoclimate records (Carlson et al., 2008a,b; LeGrande and Schmidt, 2009). We have selected terrestrial data that provide a proxy of the δ^{18}O in precipitation (hereafter δ^{18}Oa) throughout the LGM and deglacial climate (see Table 2 for list of δ^{18}O proxy records used in this analysis). To estimate LGM and deglacial δ^{18}O in the ocean (hereafter δ^{18}Oo), data from ocean sediment cores with continuous coverage from the LGM to preindustrial were selected (Table 2). We used the average of all data within 1000 yr of each time slice (i.e., 20–22 ka for 21 ka, 13–15 ka for 14 ka, 2–0 ka for control) to estimate the δ^{18}Oa and δ^{18}Oo anomaly from each record for direct comparison with the model.

3 Climate changes relative to 0 ka

The main goals of this section are (1) to characterize the differences that arise in simulated climate at each time slice and (2) to focus on changes due to changes in LIS topography alone. Due to the boundary conditions forcing the glacial climate, our model results are broadly consistent with previous GCMs of the LGM (CLIMAP, 1981; Braconnot et al., 2007a), where climate anomalies and differences between simulations are minimal in the Southern Hemisphere. Therefore, we focus our attention to the Northern Hemisphere where greater variability is simulated.

3.1 Atmospheric changes

3.1.1 Surface air temperature

Both 21 simulations show global cooling with the largest surface air temperature (SAT) anomalies (21 ka minus 0 ka) in the Northern Hemisphere where LGM ice sheets exert their influence. SAT anomalies are greatest directly over the LGM ice sheets due to the large changes in elevation and albedo, but there is also substantial downstream cooling over most of northern Asia and the northern oceans (Fig. 2a). Global area-weighted mean SAT anomalies (21 ka minus control) for the 21 ka-5G and 21 ka-L simulations are $-5.1 \pm 0.1\,^{\circ}$C and $-5.4 \pm 0.1\,^{\circ}$C, respectively (unless otherwise stated, uncertainty is expressed as standard deviation across decadal variability about the 100 yr mean).

CPD
9, 3239–3306, 2013

Assessing the impact of Laurentide Ice-Sheet topography on glacial climate

D. J. Ullman et al.

This difference in SAT is significant, developing solely in response to changes in LIS boundary conditions. Since differences in SAT between our two scenarios are exacerbated directly over the LIS due to topographic differences (i.e., vertical lapse rate of temperature and an ∼ 1000 m maximum LIS height difference), the global mean SAT anomalies with the LIS area removed are −4.7 ± 0.1 °C and −5.0 ± 0.1 °C, thus suggesting that differences between the simulations are not due to differences directly over the ice sheet alone.

We use the differences in elevation and the resulting SAT at each time slice to estimate summer temperature lapse rates over the LIS by regressing the change in SAT onto the change in elevation. Using this approach, we estimate summer ice-sheet lapse rates of −4.6 °C km^{-1} for 21 ka, which is consistent with the published range of −4 to −7 °C km^{-1} of Abe-Ouchi et al. (2007), but slightly lower than earlier estimates of −6 to −8 °C km^{-1} (Marshall et al., 2000; Pollard and PMIP, 2000; Charbit et al., 2002). Applying this lapse rate over the LIS compared to modern elevation accounts for 40–50 % of the SAT anomalies over the LIS. The remaining change in SAT temperature is due to other ice-sheet impacts (i.e., albedo) and changes in atmospheric circulation.

To the extent that borehole measurements capture SAT from the LGM, our results are ∼ 1 °C colder than globally integrated borehole estimates that suggest LGM cooling of 4.3 ± 0.2 °C (Huang et al., 2008). Borehole measurements from Summit Greenland suggest LGM cooling of 14–16 °C (Cuffey et al., 1995; Cuffey and Clow, 1997), which is colder than our model anomalies of −9.9 ± 0.7 °C (21 ka-L) and −11.0 ± 0.8 °C (21 ka-5). This difference could in part be due to the smoothed topography in ModelE2-R relative to the actual elevation of the ice-core site, as well as due to differences in the temperature inversion over the ice sheet (Cuffey and Clow, 1997; Alley, 2000). An alternate estimate adjusting for possible changes in the temperature inversion over Greenland suggests that Greenland LGM cooling to be ∼ 10 °C (Alley et al., 2010). Boreholes from Germany, Slovenia, and the Czech Republic suggest LGM cooling of 7–10 °C (Safanda and Rajver, 2001), which agree with our model anomalies of −10.1 ± 0.7 °C (21 ka-L) and −9.5 ± 0.6 °C (21 ka-5G).

CPD
9, 3239–3306, 2013

As we will show later (Sect. 4.1), large differences exist between LIS scenarios in both time slices, particularly in Northeast Asia, Beringia, and the North Pacific. We therefore focus on temperature proxies from this region that help to constrain the differences. Proxy records from this region are limited, but one recent modern analog approach based on pollen spectra from Lake El'gygytgyn in Northeast Siberia suggests that the mean temperature of the warmest month (July) at 20 ka is ~ 6 °C colder than present (Melles et al., 2012), whereas the model results in a cooling of July temperatures by 16.5 ± 1.1 °C (21 ka-L) and 12.8 ± 0.7 °C (21 ka-5G). Model results appear to be much too cold in this region, but the lake record may not extend far enough back to capture full LGM cooling, and lake ice permanence at the LGM may have strongly limited pollen transport into the lake during this time, biasing the record towards warm years (Melles et al., 2007, 2012). One SAT reconstruction from fossil lipids in paleosols of East Asia suggests LGM summer cooling of 8–10 °C (Peterse et al., 2011), whereas our 21 ka simulations suggest summer cooling of 9.0 ± 0.7 °C (21 ka-L) and 8.1 ± 0.4 °C (21 ka-5G). Reconstructions from Zagoskin and Burial Lakes in Northwestern Alaska suggest July LGM cooling of 4 ± 1.6 °C and 5 ± 1.6 °C, respectively, which is consistent with general LGM cooling of the region (Viau et al., 2008; Kurek et al., 2009). Our 21 ka simulations suggest July LGM cooling of 8.8 ± 0.9 °C (21 ka-L) and 4.6 ± 0.4 °C (21 ka-5G) for Zagoskin Lake, and 12.2 ± 1.0 °C (21 ka-L) and 8.5 ± 0.7 °C (21 ka-5G) for Burial Lake.

For the 14 ka simulations, SAT anomalies continue to be negative (Fig. 3a), with global mean SAT anomalies of −3.0 ± 0.1 °C (14 ka-L) and −2.8 ± 0.1 °C (14 ka-5G). These values are consistent with the global integrated borehole estimate of −2.9 ± 0.6 °C for the same time period (Huang et al., 2008). Data from Summit Greenland suggest 14 ka cooling of 7–9 °C (Cuffey and Clow, 1997), which is comparable with our 14 ka anomalies at this location of −6.4 ± 0.7 °C (14 ka-L) and −6.9 ± 0.6 °C (14 ka-5G). The greatest cooling occurs directly over the ice sheets with downstream cooling by as much as 10 °C over northern Asia (Fig. 3a). Again, we estimate a summer ice-sheet lapse rate of ~ 4.8 °C km^{-1} over the LIS (calculated by regressing change in SAT onto change in elevation between 14 ka-L and 14 ka-5G, as above), which is consistent with values from the 21 ka simulations.

Downstream SAT differences between LIS scenarios still exist at 14 ka (see Sect. 4.1.1), so we continue to focus our temperature comparisons on this region. Model results suggest a July SAT change in this location of $-0.8 \pm 0.7\,^{\circ}$C (14 ka-L) and $+0.6 \pm 0.9\,^{\circ}$C (14 ka-5G), consistent with the record at Lake El'gygytgyn suggesting July temperatures near modern conditions at 14 ka (Melles et al., 2012). The other proxy records from East Asia and Northwest Alaska suggest SAT near present conditions ($\pm 1.6\,^{\circ}$C; Peterse et al., 2011; Viau et al., 2008; Kurek et al., 2009). Our model results indicate colder 14 ka anomalies of $-2.7 \pm 0.5\,^{\circ}$C (14 ka-L) and $-2.0 \pm 0.8\,^{\circ}$C (14 ka-5G) for East Asia, $-2.0 \pm 0.6\,^{\circ}$C (14 ka-L) and $-1.5 \pm 0.7\,^{\circ}$C (14 ka-5G) for Zagoskin Lake, and $-2.6 \pm 0.7\,^{\circ}$C (14 ka-L) and $-1.9 \pm 0.7\,^{\circ}$C (14 ka-5G) for Burial Lake.

3.1.2 Precipitation minus evaporation

At 21 ka and 14 ka, precipitation is largely diminished, reflecting the decrease in atmospheric water vapor (global mean specific humidity anomalies of −20.2, −19.6, −11.9, and −11.4 g water vapor per kg dry air for 21 ka-L, 21 ka-5G, 14 ka-L, 14 ka-5G, respectively, tracking relative anomalies in global mean temperature). In general, the largest precipitation minus evaporation (P–E) anomalies occur in the tropics (Fig. 2b and b) reflecting a southward displacement of the Inter-Tropical Convergence Zone (ITCZ) as seen by the P–E over the tropical Pacific, Atlantic, South America, and Africa. This shift in the ITCZ is consistent with models and proxy records of the glacial hydrologic cycle (e.g., Peterson et al., 2000; Thompson et al., 2000; Chiang et al., 2003; Wang et al., 2004; Broccoli et al., 2006; Braconnot et al., 2007b).

In all simulations, enhanced precipitation over the Indonesian archipelago and the Arafura Sea north of Australia is likely due to a too large of land-sea contrast in ModelE2, with enhanced drying over the surrounding water masses. This feature likely traces back to too many low clouds in the tropics in ModelE2. This is not unique to

CPD
9, 3239–3306, 2013

these simulations and exists in all the CMIP5 runs by ModelE2; newer versions of ModelE2 have addressed this issue (delGenio personal communication, 2013). The lower sea level also subaerially exposes much of this region, contributing to this enhanced precipitation.

3.1.3 δ^{18}O of the atmosphere

LGM δ^{18}Oa anomalies largely reflect the reduction in SAT, with the greatest depletion in δ^{18}O occurring directly over the ice sheets and across northern Asia (Fig. 2a and c). However, this direct coupling of SAT and δ^{18}Oa does not hold everywhere. Areas of slight enrichment occur over nearly all tropical oceans basins in regions of reduced precipitation (Fig. 2b), despite globally colder SAT. In contrast, 21 ka anomalies are particularly depleted over northern Australia and into Indonesia where there is enhanced P–E.

Direct comparison of the simulated change in δ^{18}Oa relative to 0 ka with terrestrial records that span this period shows that the 21 ka simulations capture the general change in δ^{18}Oa where such proxy records exist (see colored dots in Fig. 2c). However, the simulations seem to do poorly in capturing the tropical speleothem records that are heavily influenced by precipitation seasonality (Wang et al., 2001; Bar-Matthews et al., 2003; Holmgren et al., 2003; Dykoski et al., 2005; Partin et al., 2007; Cheng et al., 2012). Despite this bias, the δ^{18}Oa anomalies of 21 ka-L and 21 ka-5G correlate well with these data with $r = 0.72$ and $r = 0.67$, respectively (correlations are significant with $p \leq 0.01$).

The δ^{18}Oa anomalies at 14 ka also reflect the reduction in SAT, particularly over the Northern Hemisphere ice sheets and northern Asia (Fig. 3a and c). The enrichment of δ^{18}Oa over the tropical oceans is no longer evident, but the 14 ka depletion over northern Australia and into Indonesia still persists in concert with the enhanced P–E anomaly (Fig. 3b). The comparison with proxy data again captures the general spatial trends in 14 ka δ^{18}Oa anomalies (Fig. 3c). There is still some poor mismatch with some of the in the tropical records, but the 14 ka-L simulation still correlates well with

CPD
9, 3239–3306, 2013

the proxy measurements ($r = 0.6$, $p \le 0.05$). However, the correlation of 14 ka-5G is not as strong and is less significant ($r = 0.4$, $p = 0.19$). Unfortunately majority of proxy records are concentrated where modeled anomalies are small, thus limiting the testing of the model results. Proxy records from northern Asia would be a better test of the models ability to capture large trends in δ^{18}Oa.

3.1.4 Circulation and pressure

The emplacement of the LIS and an enhanced Northern Hemisphere equator-pole temperature gradient at both 21 ka and 14 ka sets of simulations result in the strengthening and southward shift of the polar jet (Fig. 2e), as in previous simulations (Kageyama et al., 1999; Arpe et al., 2011; Hofer et al., 2012). In addition, the north-south Rossby wave nature of the jet appears to be enhanced, particularly downstream of the ice sheets, reflecting greater instability in the mean state of the jet (Donohoe and Battisti, 2009). This shift in jet location influences surface winds with enhancement over much of the North Atlantic and North Pacific (Fig. 2d). In the Southern Hemisphere, however, there is a weakening of the subtropical jet, relative to 0 ka, and surface wind anomalies are diminished.

At 14 ka, both simulations continue to have a southward shift in the polar jet (Fig. 3e). The anomalies are more zonal than in the 21 ka simulations, suggesting that Rossby Waves in the 14 ka jets is more similar to the control simulation. The southward displacement and enhancement of the polar jet over the midlatitudes leads to elevated surface winds across much of the North Atlantic and into western Asia (Fig. 3d). Again, in the Southern Hemisphere, the subtropical jet is largely reduced relative to the control simulation.

Upper level air pressure is associated with these changes in atmospheric circulation as well as changes in SAT. In general, the enhanced zonal mean meridional temperature gradient during the glacial simulation drives a lowering of 500 mb geopotential heights in the higher latitudes. However, removing the zonal mean in the 500 mb heights reveals a series of planetary waves from west to east (Fig. 2f) that are reflected

CPD
9, 3239–3306, 2013

in the meridional wave nature of the atmospheric jet (Fig. 2e). Most notably, the 21 ka simulations show a deepening of a trough immediately downstream of the LIS, as well as an enhanced trough over eastern Asia and an enhanced ridge over Beringia, immediately upstream of the LIS. Previous sensitivity experiments testing the impact of LGM ice sheet elevation on atmospheric circulation have described similar patterns in geopotential heights as the "stationary wave effect" (Broccoli and Manabe, 1987; Cook and Held, 1988; Abe-Ouchi et al., 2007). The 500 mb height anomalies in the 14 ka simulations reflect a similar pattern of stationary wave generation with deepening of troughs immediately downstream of the LIS and Scandinavian Ice Sheet and an enhanced ridge immediately upstream of the LIS (Fig. 3f).

3.1.5 Albedo

Surface albedo anomalies at 21 ka reflect the colder Northern Hemisphere temperatures and enhanced perennial snow cover over the ice sheets and across northern Asia (Fig. 2g). In addition, the expansion of sea ice in the Nordic Seas and the Northwest Pacific leads to an increase in surface albedo (Fig. 2g). Planetary albedo largely shows the same pattern as ground albedo, indicating that changes in shortwave reflectivity is primarily driven by surface cover changes instead of cloud cover (Fig. 2h).

Surface albedo at 14 ka is also enhanced directly over the ice sheets as well as across northern Asia, where there continues to be greater duration of seasonal snow cover relative to 0 ka (Fig. 3g). Elevated albedo over the Nordic Seas is again associated with sea ice expansion in this region, and the trends in ground albedo are largely mimicked by planetary albedo (Fig. 3h), suggesting that changes in low clouds only play a minor role on the total albedo anomaly.

Discussion Paper | Discussion Paper | Discussion Paper | Discussion Paper |

CPD

9, 3239–3306, 2013

Assessing the impact of Laurentide Ice-Sheet topography on glacial climate

D. J. Ullman et al.

3.2 Ocean changes

3.2.1 Ocean temperature

Similar to SAT, global sea surface temperatures (SST) are colder in the 21 ka simulations, with particularly strong cooling over the North Pacific (Fig. 4a). Some proxy reconstructions have suggested warmer than present conditions in this region (CLIMAP, 1981; Waelbroeck et al., 2009), but most recent GCM simulations do not have this feature (Braconnot et al., 2007a). The warmer than present interpretation may be a result of no-analogue issues with foraminifera transfer functions (Mix et al., 1999), or a limitation in LGM simulations.

The 21 ka simulations capture the general range of mean SST estimates from the Multiproxy Approach for the Reconstruction of the Glacial Ocean Surface (MARGO) proxy data in both the Pacific and Atlantic basins (Fig. 5a and b; Waelbroeck et al., 2009). The large differences between the simulations in the North Pacific indicates that this is a sensitive region for testing the model results. SST proxy records are sparse from the North Pacific, but limited data seem to indicate colder conditions. Alkenone and transfer function SST reconstructions from off the coast of Oregon document LGM cooling of 4–7 °C (Doose et al., 1997; Ortiz et al., 1997; Mangelsdorf et al., 2000; Herbert et al., 2001; Rosell-Melé et al., 2004), which are more consistent with the 21 ka-L result of 4.0 ± 0.3 °C cooling than with the 21 ka-5G cooling of 3.1 ± 0.2 °C. Alkenone records from the Sea of Okhotsk suggest LGM SST cooling of only 0–1 °C (Harada et al., 2006; Seki et al., 2004). The 21 ka-5G simulation has LGM cooling of 4.6 ± 0.2 °C in this region, and the 21 ka-L simulation shows cooling of 7.4 ± 0.2 °C, suggesting that neither simulation adequately captures SST in this somewhat isolated basin.

This cooling in 21 ka-L extends throughout the entire ocean with total global mean ocean temperature anomalies of −2.15 ± 0.01 °C (21 ka-L) and −2.01 ± 0.01 °C (21 ka-5G) (global mean ocean temperatures are scaled by mass of ocean water). Additionally, the greater global cooling in 21 ka-L persists in the deep ocean where tempera-

CPD
9, 3239–3306, 2013

ture anomalies averaged over the bottom 2000 m are −1.18 ± 0.01 °C (21 ka-L) and −1.04 ± 0.01 °C (21 ka-5G). The global mean ocean anomalies overlap with Kr/N_2 estimates of global mean ocean cooling at the LGM of 2.7 ± 0.6 °C (Headly and Severinghaus, 2007).

At 14 ka, cold SST anomalies continue throughout the global oceans, again with particular cooling in the North Pacific (Fig. 6a). The 14 ka basin-wide transects of SST show a similar pattern to 21 ka, with only slightly negative anomalies throughout most of the southern and tropical regions of the basins and larger cooling north of 40° N (Fig. 5c and d). Unfortunately, a SST compilation analogous to MARGO is not available for 14 ka, but the strong cooling in the North Pacific continues to suggest this region's importance, despite a limited number of SST records from this region. Three records from off the coast of Japan show mean 14 ka SST cooling of 1–3 °C (Sawada and Handa, 1998; Sun et al., 2005; Yamamoto et al., 2005). Our 14 ka simulations are consistent with cooling of 2.1 ± 0.2 °C (14 ka-L) and 2.0 ± 0.2 °C (14 ka-5G) in the same region. Model SST is too cold in the Sea of Okhotsk but within the uncertainty of proxy measurements, where alkenone records suggest SST cooling of 0–4 °C (Harada et al., 2006; Seki et al., 2007), compared with 4.3 ± 0.2 °C (14 ka-5G) and 4.7 ± 0.2 °C (14 ka-L). Additionally, one alkenone record from the southeastern Bering Sea suggests a SST cooling of 1–4 °C (Caissie et al., 2010; Dubois et al., 2009), while the 14 ka simulations indicate SST cooling of 5.2 ± 0.5 °C (14 ka-5G) and 5.6 ± 0.4 °C (14 ka-L).

Total global mean ocean anomalies are again colder at in the 14 ka-L simulation with anomalies of −0.83 ± 0.1 °C (21 ka-L) and −0.71 ± 0.1 °C (21 ka-5G). In the deep ocean (bottom 2000 m), however, temperature is nearly consistent with 0 ka with anomalies of −0.09 ± 0.01 °C (14 ka-L) and +0.05 ± 0.01 °C (14 ka-5G).

3.2.2 Sea surface salinity

Globally averaged sea surface salinity (SSS) anomalies at 21 ka (+0.55 ± 0.01 psu for 21 ka-L; +0.60 ± 0.01 psu for 21 ka-5G) reflect a generally more saline ocean related to the reduction in global ocean volume. However, there are prominent regional distinc-

CPD
9, 3239–3306, 2013

tions in SSS anomalies (Fig. 4b), such as the increase in SSS across the Arctic Ocean that is related to the increase in sea ice formation and brine rejection, as shown in previous LGM simulations (Otto-Bliesner et al., 2006). The freshening in the Gulf of Mexico and along the Scandinavian margin reflects the increased contribution of glacial runoff, which is consistent with SSS reconstructions (de Vernal et al., 2000; Flower et al., 2004). In addition, prominent freshening in the Sea of Japan is also consistent with reconstructions (Keigwin and Gorbarenko, 1992; Tada et al., 1999; Gorbarenko and Southon, 2000) and reflects the elevated P–E anomalies (Fig. 2b), as well as the isolation of the basin from the open ocean due to sea-level lowering. The reduction in 21 ka SSS in the South China and Arafura Seas is also linked to P–E anomalies in the 21 ka simulations (Fig. 2b). SSS anomalies from the South China Sea have been associated with greater proximity to river outlets (Steinke et al., 2006). This may confirm that P–E anomalies are too high in this region from an elevated land-sea temperature contrast in the model (see Sect. 3.1.2).

Average SSS anomalies at 14 ka are +0.17 ± 0.01 psu (14 ka-L) and +0.19 ± 0.01 psu (14 ka-5G), continuing to suggest a more saline surface ocean related to volumetric changes in the global ocean. The Arctic Ocean is now dominated by the freshening of surface waters relative to 0 ka (Fig. 6b), as the Northern Hemisphere ice sheets supply a greater amount of meltwater and river routing to the region (not shown). In addition, the Gulf of Mexico and eastern North Atlantic reflects continued meltwater runoff from the southern LIS as inferred from proxies from the region (Flower et al., 2004) as well as sustained freshening in the Nordic Seas (de Vernal and Hillaire-Marcell, 2000). The Sea of Japan continues to have prominent fresh SSS anomalies due to enhanced P–E and limited open ocean exchange, contrary to observations (Gorbarenko and Southon, 2000).

3.2.3 δ^{18}O of the surface ocean

21 ka δ^{18}Oo anomalies largely reflect the trends in SSS, with nearly global enrichment in the open ocean due to sea-level lowering from increased LGM ice-sheet volume.

CPD
9, 3239–3306, 2013

More localized effects include δ^{18}Oo enrichment in the Arctic Ocean concurrent with elevated sea ice formation and δ^{18}Oo depletion in the Gulf of Mexico and along the Scandinavian Ice Sheet margin where there is an increase in meltwater runoff relative to 0 ka (Fig. 4c). The 21 ka δ^{18}Oo anomalies also show depleted values in the Sea of Japan.

We compare the simulated change in δ^{18}Oo relative to 0 ka using marine sediment records of foraminifera that have an independent temperature reconstruction from the same core to correct for glacial changes in SST (i.e., δ^{18}O of seawater, see Sect. 2.5). The 21 ka simulations capture the general change in δ^{18}Oo shown from the proxy data (Fig. 4c). One noticeable offset is in the Gulf of Mexico where the Ziegler et al. (2008) record in the Gulf of Florida sub-basin is not significantly influenced by LIS runoff, whereas ModelE2-R simulates a significant impact of LIS runoff consistent with other Gulf of Mexico records (Flower et al., 2004). Unfortunately, the limited number of temperature-corrected δ^{18}Oo records that meet our selection criteria (providing data from the LGM as well as the past 2000 yr) are primarily confined to the tropics. We therefore include these data with our δ^{18}Oa records for a global comparison of oxygen δ^{18}O at the LGM. Despite the limitations in spatial resolution of this dataset, the 21 ka-L and 21 ka-5G simulations correlate moderately well with the total δ^{18}O proxy dataset, with $r = 0.53$ and $r = 0.62$ respectively ($p \leq 0.01$ for both).

The 14 ka δ^{18}Oo anomalies also reflect the general trends in SSS (Fig. 6b and c). The freshening of the Arctic Ocean from glacial meltwater runoff leads to depleted δ^{18}Oo values relative to 0 ka. The 14 ka simulations capture the general trends in the tropics-dominated proxy dataset, and the inclusion of these data into a total 14 ka δ^{18}O comparison result in correlations for 14 ka-L and 14 ka-5G of $r = 0.41$ and $r = 0.41$, respectively ($p \leq 0.01$).

CPD
9, 3239–3306, 2013

3.2.4 Sea ice

There is expansion of annually averaged sea ice in the Nordic and Labrador Seas in the 21 ka simulations relative to the control (Fig. 4d), and this extent is largely the same as the maximum wintertime extent (not shown). In the Nordic Sea, the sea ice increases are primarily confined to north of Iceland. This sea ice extent is largely consistent with proxy inferences of wintertime sea ice extent from this region (Sarnthein et al., 2003), but we do not capture the summer sea ice pullback of this reconstruction. In the Labrador Sea, ice extends from just south of Hudson Strait to the southwest coast of Greenland, which is consistent with perennial sea-ice reconstructions (de Vernal and Hillaire-Marcell, 2000; de Vernal et al., 2000) and previous LGM simulations (Otto-Bliesner et al., 2006, 2007; Braconnot et al., 2007a). The other region of major sea ice expansion in the 21 ka simulations occurs in the Sea of Okhotsk and the Bering Sea (Fig. 4d), also consistent with reconstructions (Shiga and Koizumi, 2000; Katsuki et al., 2010; Caissie et al., 2010).

The 14 ka simulations also have expansion of sea ice into the Nordic Sea, Sea of Okhotsk, and Bering Sea (Fig. 6d). Unfortunately there is no basin-wide reconstruction of 14 ka sea ice in the North Atlantic, although it was largely reduced to the Fram Strait by the start of the Holocene (de Vernal et al., 2008). Reconstructions from the Sea of Okhotsk suggest persistent sea ice in the region until after 6.5 ka, but the Bering Sea likely began to transition away from perennial sea ice after 17 ka (Caissie et al., 2010). However, summer sea ice extent in the Bering Sea in the 14 ka simulations is largely the same as the 0 ka simulation (not shown), consistent with this loss of perennial sea ice.

3.2.5 Ocean circulation

North Atlantic Deep Water (NADW) production is enhanced in the 21 ka simulations at the mid-latitudes (up to 50° N) but diminished at higher latitudes (50–65° N) due to a southward shift in convection sites (Fig. 4e). This is associated with a deepening and strengthening of overall mean AMOC transport to 30.8 ± 0.6 Sv (21 ka-L) and 33.2 ± 0.7 Sv (21 ka-5G), relative to 28.2 ± 0.7 in the control simulation. Below the NADW, however, is an enhanced contribution of Antarctic Bottom Water (AABW) from the south (Fig. 4e). In the Pacific, the 21 ka simulations show enhanced deepwater circulation from AABW and a reduction in North Pacific Intermediate Water (NPIW; Fig. 4f).

Kinematic and water mass proxy records continue to refine reconstructions of the AMOC at the LGM, with overturning strength anywhere from 30–40 % weaker than present (McManus et al., 2004), to about the same as today (Lynch-Stieglitz et al., 2007; Ritz et al., 2013), and even the possibility of more rapid overturning at the LGM (Gherardi et al., 2009; Lippold et al., 2012). Water mass tracers suggest the shoaling of glacial NADW and a greater contribution of AABW (Curry and Oppo, 2005), but this increased stratification may also imply a more vigorous AMOC. At present, proxy uncertainty may preclude determination of whether the LGM AMOC was different than modern (Burke et al., 2011). Such uncertainty in circulation strength and depth is mirrored in a diverse array of AMOC results, some of which present stronger AMOC during the LGM (Otto-Bliesner et al., 2007) similar to our results. In the Pacific, the expansion of enriched δ^{13}C throughout the deep ocean suggests the increased influence of Antarctic-sourced waters in this basin (Matsumoto et al., 2002; Herguera et al., 2010). Other North Atlantic simulations have shown that enhanced AMOC is associated with the strengthening of the deep ocean circulation in the Pacific (Chikamoto et al., 2012), which is consistent with the enhanced negative stream function in our 21 ka results (Fig. 4f).

The 14 ka simulations also have enhanced NADW formation with a southward shift in convection sites (Fig. 6e). The location of maximum AMOC is approximately at the same depth as the control simulation, but overall mean transport remains elevated at 30.5 ± 0.6 Sv (14 ka-L) and 32.7 ± 0.7 Sv (14 ka-5G), relative to the control (28.2 ± 0.7 Sv). Again, below the NADW, there is an enhanced contribution of AABW. In the Pacific, Antarctic Intermediate Water (AAIW) formation is slightly enhanced and NPIW is reduced relative to the control (Fig. 6f).

Proxy records suggest that 14 ka AMOC strength was similar to that of the LGM (McManus et al., 2004; Lynch-Stieglitz et al., 2007). However, other records suggest a more intermediate rate of overturning in shallower waters between the relatively elevated values of the LGM and the reduced values in the Holocene (Gherardi et al., 2009). In the Pacific, overturning at 14 ka was in the middle of the transition from glacial to modern conditions (Herguera et al., 2010), which is similar to our results.

4 Ice sheet topography and resulting climate differences

Our 21 and 14 ka simulations result in distinct differences from the 0 ka control due to glacial boundary conditions that are distinct from the modern. The remainder of this paper will focus on the differences between the two simulations at each time slice that arise due to changes in LIS boundary conditions alone. Since most of the climate differences directly over the ice sheet are due to orographic differences alone, we focus on the LIS impacts in other regions.

4.1 Atmosphere differences

4.1.1 Surface air temperature

Global mean SAT anomalies are significantly different between the two simulations at 21 ka (Fig. 7a). This difference is robust even after removing the region of the LIS in the global mean, suggesting that mean SAT differences are not due to SAT directly over the LIS, but rather cooling in other regions that significantly impact the global mean. Indeed, there are prominent downstream differences in SAT, particularly over Northeast Asia and the North Pacific where 21 ka-L is 6–9 °C colder than 21 ka-5G (Fig. 7a). In addition, there is slight SAT cooling in 21 ka-L over the Gulf of Mexico and southwestern Europe. Immediately downwind of the ice sheet over Greenland, the 21 ka-L simulation shows slightly warmer SAT.

CPD
9, 3239–3306, 2013

While global mean SAT anomalies are indistinct at 14 ka, there are still regional distinctions between the simulations. Cooling over Northeast Asia and the North Pacific continues to occur in the 14 ka-L simulation relative to 14 ka-5G by 1–2 °C (Fig. 8a). Additionally, SATs are cooler over most of Europe in 14 ka-L but warmer over the Nordic Sea east of Iceland.

4.1.2 Precipitation minus evaporation

The location of the ITCZ is consistent between 21 ka-L and 21 ka-5G, but 21 ka-L presents greater precipitation north of the equator in the tropical Pacific (Fig. 7b). The 21 ka-5G simulation shows greater precipitation over the northern mid-latitude Pacific and across eastern America, south of the LIS.

At 14 ka, differences in P–E between simulations are small, but highlight a slight enhancement of Pacific precipitation south of the equator in 14 ka-5G (Fig. 8b). Differences in precipitation also occur over the North Atlantic, with drier conditions in 14 ka-L along the east coast of North America and the Atlantic coast of Europe and slightly wetter conditions in the interior of the North Atlantic.

4.1.3 δ^{18}O of the atmosphere differences

Differences in δ^{18}Oa largely reflect the differences in SAT, with the greatest relative depletion of 21 ka-L occurring in Northeast Asia and the North Pacific, where SATs show the greatest cooling relative to 21 ka-5G (Fig. 7c). In the 14 ka simulations, there is a decoupling between the differences in SAT and the differences in δ^{18}Oa, with relatively enriched δ^{18}Oa in 21 ka-L across Northeastern Africa and into south-central Asia (Fig. 8c). Additionally, the 21 ka-L shows relatively enriched values across much of the Arctic, but depleted values immediately downwind of the LIS and over southern Greenland.

CPD
9, 3239–3306, 2013

4.1.4 Atmospheric circulation

The Northern Hemisphere subpolar jet in 21 ka-5G is stronger and more zonal across the mid-latitude Pacific and to the south of the LIS (Fig. 7e). In contrast, the subpolar jet in 21 ka-L is more wave-like and lies to the north of the 21 ka-5G jet across most of Asia and the Pacific. Differences in surface wind speed reflect this jet displacement, particularly over the North Pacific, where the more northern 21 ka-L jet results in greater surface winds. Across much of the North Atlantic, 21 ka-5G surface winds are stronger than 21 ka-L, where both simulations are already enhanced relative to 0 ka (Fig. 2d).

Differences in 500 mb height between the two 21 ka simulations express a shift in the location and depth of the dominant stationary wave patterns, particularly over Siberia and Beringia, where 21 ka-L heights are substantially lower than those in the 21 ka-5G simulation (Fig. 7f). These lower heights in 21 ka-L reflect a deepening of the trough over eastern Asia and a weakening of the ridge over Beringia relative to 21 ka-5G. This general reduction of 500 mb heights across this region provide a greater influence of Arctic air masses that help to drive the colder SAT (Sect. 4.1.1).

The higher LIS in 14 ka-5G still induces an increase in jet speed and southward displacement of the polar and subtropical jets relative to 14 ka-L (Fig. 8e). However the stronger subpolar jet in 14 ka-5G now extends further to the north over northern Europe. The general differences in 500 mb heights and the implied stationary wave pattern in the 21 ka simulations still exists between the 14 ka simulations, with a continued lowering of 14 ka-L 500 mb heights in Northeast Asia and Beringia that is associated with the colder SAT in this region relative to 14 ka-5G (Fig. 8f).

4.1.5 Albedo

The 21 ka-L simulation presents a region of higher albedo in Northeastern Asia, where there is additional snow cover over Siberia and Beringia, along with a relative expansion of sea ice over the Sea of Okhotsk (Fig. 7g). The 21 ka-5G has a higher albedo in a region along the southern margin of the LIS, likely due to the southward tracking of the

CPD
9, 3239–3306, 2013

subpolar jet and enhanced snowfall. The disparity in the area extent of these albedo changes results in globally averaged ground albedo of 18.5 % for 21 ka-L compared with 18.1 % for 21 ka-5. Planetary albedo differences mimic the ground albedo differences (Fig. 7h), although cloud cover over the region in Northeast Asia is enhanced by 8–10 % in the 21 ka-L simulation (not shown).

At 14 ka, surface albedo is largely the same between the two simulations, except for the expansion of sea ice over the Nordic Seas in 14 ka-5G, which drives an increase in albedo relative to 14 ka-L (Fig. 8g). Globally averaged ground albedo is 16.4 % for 14 ka-L and 16.3 % for 14 ka-5G. Again, planetary albedo differences mimic ground albedo differences suggesting the prominence of surface albedo changes in overall albedo (Fig. 8h), with cloud cover differences of less than 2 %.

4.2 Ocean differences

4.2.1 Ocean temperature differences

Differences in SST between the 21 ka-L and 21 ka-5G simulations correlate with SAT differences (Figs. 7a and 9a), particularly in the North Pacific, Sea of Okhotsk, and Bering Sea, where 21 ka-L simulates colder SST by up to 3.5 °C. Averaged globally, SST anomalies are slightly colder in 21 ka-L (−2.7 ± 0.1 °C) compared with 21 ka-5G (−2.5 ± 0.1 °C).

Differences between the 14 ka simulations are most pronounced over the Northwest Atlantic and the North Pacific (Fig. 10a), where 14 ka-L SSTs are colder, similar to SAT differences over these regions (Fig. 9a). Globally averaged SST anomalies are equivalent (−1.5 ± 0.1 °C in 21 ka-L and −1.4 ± 0.1 °C in 21 ka-5G).

4.2.2 Sea surface salinity differences

Surface waters are generally fresher in 21 ka-L, particularly in the Arctic Ocean and the Gulf of Mexico, reflecting a greater contribution of LIS melt water through the MacKen-

CPD
9, 3239–3306, 2013

zie and Mississippi Rivers (Fig. 9b). 21 ka-5G presents a greater contribution of Scandinavian Ice Sheet melt water through the Ob and Yenesei Rivers leading to a localized freshening of SSS along the coast, but in general, Arctic surface waters are more saline in 21 ka-5G. North Tropical Pacific surface waters are slightly fresher in 21 ka-L in association with enhanced P–E over this region (Fig. 7b).

SSS differences at 14 ka are largely similar to those in the 21 ka simulations, with fresher waters in 14 ka-L in the Arctic Ocean, the Gulf of Mexico, and along the Atlantic coast of North America (Fig. 10b). The 14 ka-L simulation continues to present localized freshening due to greater melt water contributions of the LIS to the MacKenzie and Mississippi Rivers. SSS differences are negligible over the Pacific, reflecting the minimal changes in P–E (Fig. 8b).

4.2.3 δ^{18}O of the surface ocean differences

The differences in δ^{18}Oo at 21 ka are largely similar to the differences in SSS, with depleted values in 21 ka-L relative to 21 ka-5G across the Arctic Ocean and the Gulf of Mexico (Fig. 9c), reflecting the enhanced melt water contributions in 21 ka-L to the MacKenzie and Mississippi Rivers (Fig. 9b). In addition, 21 ka-L waters are depleted along the north shore of the Scandinavian Ice Sheet, consistent with reduced SSS and enhanced melt water contribution in 21 ka-5G along this margin. The Sea of Japan shows slightly depleted δ^{18}Oo values in 21 ka-L but no change in SSS, suggesting a shift in the isotopic composition of runoff arriving to this basin but a consistent volume of this runoff between the simulations.

In the 14 ka simulations, however, this relationship between SSS and δ^{18}Oo becomes decoupled, with fresher Arctic conditions in 14 ka-L associated with more enriched values of δ^{18}Oo relative to 14 ka-5G (Fig. 10c). However, the 14 ka-L simulation continues to show depleted values in relation to the greater contribution of fresh water from the MacKenzie and Mississippi drainage outlets. In addition, the Sea of Japan continues to reflect a difference in the isotopic composition of river runoff to the basin, but here the 14 ka-5G simulation presents depleted δ^{18}Oo values. Again, the lack of

CPD
9, 3239–3306, 2013

a SSS difference in this basin suggests that freshwater runoff is consistent between the simulations (Fig. 10b).

4.2.4 Sea ice differences

Annually averaged sea ice differences are negligible across much of the ocean basins, except in the Sea of Okhotsk and Bering Sea, where the 21 ka-L has a significant increase in sea ice over that of 21 ka-5G (Fig. 9d). The expansion of sea ice across the Nordic Seas in the 21 ka simulations relative to the control simulation is consistent between 21 ka-L and 21 ka-5G, with 21 ka-L presenting slightly greater sea ice fraction (no more than 5 %).

In the 14 ka simulation, sea ice differences are again negligible (Fig. 10d). However, at this time slice, differences in sea ice are minimized in the Sea of Okhotsk, while there are significant differences in the Nordic Seas, with enhanced sea ice in the 14 ka-5G simulation.

4.2.5 Ocean circulation differences

The 21 ka-5G simulation exhibits a stronger AMOC than 21 ka-L. The difference in AMOC stream function not only reflects the increase in AMOC transport for 21 ka-5G but also a deepening of the main overturning and a slight increase in AABW in flow (Fig. 9e). In the Pacific, the 21 ka-5G simulation shows an enhanced contribution of Antarctic Intermediate and Antarctic Bottom Waters throughout most of the basin (Fig. 9f), with the 21 ka-5G having the greatest AABW influence (i.e., deepwater stream function more negative than 21 ka-L). In addition, the 21 ka-5G also shows enhanced production of NPIW relative to 21 ka-L (or less of a reduction relative to 0 ka; see Sect. 3.2.5).

The 14 ka-5G simulation also has stronger AMOC transport, but the depth of overturning is similar to the 14 ka-L simulation (Fig. 10e). The 14 ka-5G results in a greater contribution of AABW into the deep Atlantic. In the Pacific, 14 ka-5G shows an in-

CPD
9, 3239–3306, 2013

creased contribution of AAIW, but the differences do not extend to include AABW (Fig. 10f).

5 The effects of ice-sheet topography

Uncertainty in the height of the LIS has a measurable impact on the simulated climate in GISS ModelE2-R, particularly at 21 ka, where global mean SATs are significantly different between 21 ka-L and 21 ka-5G. This response to changes in LIS topography alone is due to a series of differences in the 21 ka climate, initiated by the differences in atmospheric circulation that arise due to the enhanced topographic barrier in the LIS of 21 ka-5G. In both 21 ka simulations, the polar jet is forced to the south of the LIS (Fig. 2e). However, the elevated topographic barrier in the 21 ka-5G LIS drives the polar jet to be more zonal, whereas the 21 ka-L jet circulation has a greater meridional component reflecting a shift in the downstream stationary waves in the Northern Hemisphere relative to 21 ka-5G, as seen in 500 mb height differences (Fig. 7f). The primary impact of these stationary wave differences is downstream colder temperatures across Siberia, Beringia, and the North Pacific, leading to elevated sea ice in the Sea of Okhotsk and Bering Sea, as well as enhanced snow cover across Siberia (Figs. 2 and 9). Both of these impacts lead to an increase in ground albedo, thus reducing the total incoming shortwave budget in 21 ka-L (Fig. 7g and h). This snow cover-albedo positive feedback thus leads to further global cooling.

In the 14 ka simulations, the difference in the magnitude of maximum LIS height is smaller between the two reconstructions, but there is still downstream cooling over Siberia and Beringia in 14 ka-L related to a similar difference in atmospheric circulation and stationary waves (Fig. 3e, f). However, differences in snow cover and surface albedo are no longer present across this region (Fig. 7g), and the global mean temperatures between 14 ka-L and 14 ka-5G are equivalent. This comparison with the 21 ka simulation might suggest a minimum cutoff in LIS maximum elevation difference that induces strong enough changes in atmospheric circulation to cause significant differ-

CPD
9, 3239–3306, 2013

Assessing the impact of Laurentide Ice-Sheet topography on glacial climate

D. J. Ullman et al.

ences in global mean surface temperature through a snow-albedo feedback. However, the 14 ka simulations are also forced with elevated boreal summer insolation and greenhouse gases, such that generally warmer globally averaged temperatures at 14 ka (relative to 21 ka) may preclude the expansion of snow and sea ice in this region, eliminating the possibility of inducing this snow-albedo cooling feedback, even with the differences in planetary wave strength induced by LIS topographic differences.

Significant differences in ocean circulation also arise due changes in the LIS topography. All of our simulations show increased AMOC transport relative to the control, with southward displacement of the NADW formation (Figs. 4e and 6e). Glacial surface winds are enhanced over the North Atlantic (relative to 0 ka) in relation to the southward shift in the polar jet (Figs. 2d and 3d). Such windier conditions may provide the mechanism driving enhanced overturning in our simulations (Wunsch, 2003). In each the 21 and 14 ka simulation pairings, the higher LIS (21 ka-5G and 14 ka-5G) results in a stronger AMOC (Figs. 9e and 10e). In either case, there is no significant change in river runoff between the simulations, but both 21 ka-5G and 14 ka-5G have stronger wind speeds over the North Atlantic relative to their 21 ka-L and 14 ka-5G counterparts, leading to enhanced wind-driven overturning. These differences in AMOC strength are transferred to the deep Pacific with enhanced contribution of AAIW and AABW associated with the stronger AMOC (Chikamoto et al., 2012). Despite these changes in circulation, the 21 ka-L simulation has colder ocean temperatures (relative to 21 ka-5G) in both the globally averaged ocean and the deep ocean, suggesting ocean temperatures are reflecting the overall colder climate and reduced heat content of the system as would be expected from the snow-albedo feedback mechanism driving colder SAT.

To better constrain the range of climate variability that arise from uncertainty in LIS topography, more data are needed from regions where resulting climate differences are the greatest. The region of Siberia, Beringia, and the North Pacific have modeled differences in SAT, δ^{18}O, surface albedo, SST and sea concentrations, all related to the differences in atmospheric circulation that arise due to variation in LIS topography in both 21 and 14 ka simulations. Therefore, this region serves an important model-data

CPD
9, 3239–3306, 2013

test location on the LIS reconstructions used in GCMs. Unfortunately, the distribution of LGM SST proxy records from the North Pacific is limited (Kucera et al., 2005; Waelbroeck et al., 2009) and most records that do exist are confined along coastal regions, where GCMs may not adequately resolve changes in the Kuroshio and California Currents, and sea level boundary conditions may also significantly influence ocean current behavior (Ortiz et al., 1997; Kao et al., 2006). In addition, only a few terrestrial reconstructions of SAT and δ^{18}Oa exist from lake records in the region (Melles et al., 2012; Peterse et al., 2011; Viau et al., 2008; Kurek et al., 2009), but perennial ice cover, proxy uncertainties, and the possibility of no-analog environments in pollen reconstructions may limit the ability of such reconstructions to distinguish the climate differences discussed in this paper. Future data collection should focus on Northeast Asia and the North Pacific to help test LIS boundary conditions.

6 Implications for ice sheet stability

The extent and volume of the LIS was determined by a number of glaciological factors that impact ice sheet stability. LIS surface mass balance was paced by boreal summer insolation (Hays et al., 1976; Imbrie and Imbrie, 1980), with particular focus on the obliquity band (Huybers and Wunsch, 2005). Such continuous cycling of boreal summer insolation limits the size of the LIS through latitudinal shifts in the equilibrium line altitude moving in step with insolation (Oerlemans, 1991; Ruddiman, 2002). Ice sheet size is also limited by an ice thickness-basal melting negative feedback, whereby increases in ice thickness can lead to a decrease in the pressure melting point, decoupling the ice sheet from its bed and allowing for enhanced basal sliding and ice height drawdown (Clarke, 1987; Payne, 1995; Marshall and Clark, 2002). Such thermal instabilities may be exacerbated by subglacial till rheology conditions that might also limit ice sheet height (Clark et al., 1994; Clark and Pollard, 1998; Licciardi et al., 1998).

Our results may suggest an additional limit on LIS height. As shown in our LGM simulations, the larger LIS in 21 ka-5G leads to a warmer global mean SAT due to atmospheric circulation changes and the snow-albedo feedback in Northeast Asia. That an increase in LIS maximum height leads to global surface warming might suggest a climatically-driven negative feedback on LIS surface mass balance that limits ice sheet height above a certain threshold. Satellite-based gravity field measurements of glacial isostatic adjustment have suggested the need for revisions to ICE-5G (Peltier and Drummond, 2008; Peltier, 2009) to be included in the upcoming ICE-6G that lower maximum LIS elevation (Peltier, 2010; otherwise see PMIP3 boudary conditions, http://pmip3.lsce.ipsl.fr/). These revisions may imply that LIS elevation in ICE-5G is above the threshold of this elevation-warming feedback. In order to test this feedback mechanism, more analysis should be conducted on the impact of this SAT difference and ice-sheet topography on LIS surface mass balance.

7 Implications for testing LGM climate reconstructions

We present a range of climate variability that develops solely due to two different physically-based reconstructions of the LIS. This range of uncertainty in this boundary condition alone is enough to provide significant differences in LGM climate. Previous sensitivity experiments testing the impact of "ice" vs. "no ice" in model boundary conditions have shown large differences in LGM climate due to changes in atmospheric circulation and its attendant influence on ocean circulation (Abe Ouchi et al., 2007; Otto-Bliesner et al., 2006; Pausata et al., 2011; Hofer et al., 2012; Tharammal et al., 2012). Our 21 ka model results show that even a 20 % change in LIS elevation between two LIS reconstructions still has a similar impact on atmospheric and oceanic circulation and their influence on the LGM climate state. This suggests that the range of uncertainty within the existing LIS reconstructions can lead to significantly different results in simulated regional and global climate.

The ability of GCMs to capture LGM AMOC is often used as a test of model skill (Timm and Timmerman, 2007; Liu et al., 2009). Despite a range of proxy estimates for an AMOC target value (Yu et al., 1996; Adkins et al., 2002; McManus et al., 2004; Curry

CPD
9, 3239–3306, 2013

and Oppo, 2005; Lynch-Steiglitz et al., 2007), coupled climate models simulate different strengths and depths of the AMOC (Otto-Bliesner et al., 2007; Weber et al., 2007). The strength of the PMIP approach toward simulating the LGM is in the assessment of climate variability (i.e., AMOC) across a variety of models physics and design with a common fixed set of boundary conditions. However, our results suggest that AMOC strength in a single model may vary by nearly 10 % in response to changes in LIS topography alone, meaning that any uncertainties in the LIS boundary condition may be translated into the uncertainty in this important test of model skill. Thus, the uncertainty in the range of PMIP assessment of AMOC might be expanded with inclusion of LIS topographic uncertainty.

8 Implications for climate sensitivity

The LGM provides the most recent large-scale change in global climate and greenhouse gas concentrations through which global climate sensitivity can be assessed (Crucifix, 2006; Hansen et al., 2008; Schmittner et al., 2011; Hargreaves et al., 2012; PALAEOSENS, 2012). However, our model results suggest that significant differences in global mean temperature arise due to variability in LIS topography alone, suggesting that the use of models to constrain CO_2 sensitivity for the LGM should include some assessment of this boundary condition uncertainty in the overall range of possible sensitivity estimates. This analysis is particularly relevant in the assessment of how such uncertainty in boundary conditions leads to the development of fast feedbacks (i.e., snow-albedo) that are important in driving sensitivity (PALAEOSENS, 2012). Our 14 ka simulations show that even small differences in LIS height can lead to differences in atmospheric circulation, but these differences are not enough to initiate the snow-albedo feedback. Depending on the model (or other boundary conditions), this preconditioning may be sufficient to initiate fast-feedback mechanisms that lead to significant differences in global mean SAT, while other models may not provide the same

CPD
9, 3239–3306, 2013

response. Such a change in LIS within the uncertainty of reconstruction estimates may have a similar effect in other models.

Given such large uncertainties in the high-latitude boundary conditions and their associated impact on high-latitude climate, Hargreaves et al. (2012) instead correlated simulated LGM SAT from 20° S–30° N with the global mean SAT change from CO_2 doubling sensitivity ($2 \times CO_2$) simulations of each model in a grouping of PMIP2/CMIP3 pairings, which circumvented earlier issues with correlating global LGM SAT with $2 \times CO_2$ simulations (Crucifix, 2006). Our results suggest an additional source of high-latitude variability in LGM SAT that arises due to uncertainty in LIS topography alone, giving credence to the former study's focus on tropical SAT at the LGM to constrain CO_2 sensitivity. On the contrary, this additional source of uncertainty from ice-sheet topography in a region where LGM SAT anomalies are already at their greatest may suggest that focusing on the tropics could underestimate the full range of uncertainty in CO_2 sensitivity estimates.

9 Uncertainty in other boundary conditions

Finally, we have only assessed the impact of changing LIS height in one GCM. A number of the other LGM boundary conditions have been shown to significantly impact the global mean climate state, particularly the dust/aerosol forcing (Penner et al., 2004; Lohmann and Feichter, 2005; Forster et al., 2007; Chylek and Lohmann, 2008) and vegetation land cover (Jahn et al., 2005). The large range of uncertainties in both the LGM and deglacial dust forcing (Petit et al., 1981; Thompson et al., 1995; Mahowald et al., 1999; Reader et al., 1999; Power et al., 2008) and vegetation dynamics (Jackson et al., 2000; Prentice et al., 2000; Harrison et al., 2001; Ray and Adams, 2001; Bigelow et al., 2003; Williams, 2003; Pickett et al., 2004; Williams et al., 2011) suggests the need to determine the sensitivity of the climate response to the uncertainties in these boundary conditions. Future sensitivity studies will have offline coupling of ModelE2 boundary conditions to the Lund–Potsdam–Jena (LPJ) dynamic vegetation model (Sitch et al., 2003; Gerten et al., 2004; Bondeau et al., 2007) to assess the impact of this land surface choice.

10 Conclusions

We attempt to assess the range of climate uncertainty that results from variability in the possible reconstructions of the LIS elevation at two different time slices, 21 ka and 14 ka. The simulated climate at each time slice results in significant differences in atmospheric and oceanic climate. In particular, the 21 ka-L is significantly colder than the 21 ka-5G simulation in both SAT and ocean temperatures, which is due to a snow-albedo feedback in Northeast Asia that reduces the shortwave contribution to the system. Additionally, the two LIS simulations at each time slice result in significant differences in the AMOC, suggesting that any given model's ability to capture LGM anomalies in ocean overturning may be influenced as much by the LIS boundary condition as by limitations in model physics. Future research should work on minimizing the uncertainty in the LIS reconstructions, thus reducing their impact on the uncertainty in simulated glacial climate.

References

Abe-Ouchi, A., Segawa, T., and Saito, F.: Climatic Conditions for modelling the Northern Hemisphere ice sheets throughout the ice age cycle, Clim. Past, 3, 423–438, doi:10.5194/cp-3-423-2007, 2007.

Adkins, J. F., McIntyre, K., and Schrag, D. P.: The salinity, temperature, and δ^{18}O of the glacial deep ocean, Science, 298, 1769–1773, doi:10.1126/science.1076252, 2002.

Alley, R. B.: The Younger Dryas cold interval as viewed from central Greenland, Quaternary Sci. Rev., 19, 213–226, doi:10.1016/S0277-3791(99)00062-1, 2000.

Alley, R. B. and Clark, P. U.: The deglaciation of the Northern Hemisphere: a global perspective, Annu. Rev. Earth Pl. Sc., 27, 149–182, doi:10.1146/annurev.earth.27.1.149, 1999.

Alley, R. B., Andrews, J. T., Brigham-Grette, J., Clarke, G. K. C., Cuffey, K. M., Fitzpatrick, J. J., Funder, S., Marshall, S. J., Miller, G. H., Mitrovica, J. X., Muhs, D. R., Otto-Bliesner, B. L., Polyak, L., and White, J. W. C.: History of the Greenland Ice Sheet: paleoclimatic insights, Quaternary Sci. Rev., 29, 1728–1756, doi:10.1016/j.quascirev.2010.02.007, 2010.

Anderson, J. B., Shipp, S. S., Lowe, A. L., Wellner, J. S., and Mosola, A. B.: The Antarctic Ice Sheet during the Last Glacial Maximum and its subsequent retreat history: a review, Quaternary Sci. Rev., 21, 49–70, doi:10.1016/S0277-3791(01)00083-X, 2002.

Argus, D. F. and Peltier, W. R.: Constraining models of postglacial rebound using space geodesy: a detailed assessment of model ICE-5G (VM2) and its relatives, Geophys. J. Int., 181, 697–723, doi:10.1111/j.1365-246X.2010.04562.x, 2010.

Arpe, K., Leroy, S. A. G., and Mikolajewicz, U.: A comparison of climate simulations for the last glacial maximum with three different versions of the ECHAM model and implications for summer-green tree refugia, Clim. Past, 7, 91–114, doi:10.5194/cp-7-91-2011, 2011.

Arzel, O., England, M. H., and Sijp, W. P.: Reduced Stability of the Atlantic Meridional Overturning Circulation due to Wind Stress Feedback during Glacial Times, J. Climate, 21, 6260–6282, doi:10.1175/2008JCLI2291.1, 2008.

Bar-Matthews, M., Ayalon, A., Gilmour, M., Matthews, A., and Hawkesworth, C. J.: Sea–land oxygen isotopic relationships from planktonic foraminifera and speleothems in the Eastern Mediterranean region and their implication for paleorainfall during interglacial intervals, Geochim. Cosmochim. Acta, 67, 3181–3199, 2003.

Bemis, B. E., Spero, H. J., Bijma, J., and Lea, D. W.: Reevaluation of the oxygen isotopic composition of planktonic foraminifera: experimental results and revised paleotemperature equations, Paleoceanography, 13, 150–160, 1998.

Bennike, O. and Björck, S.: Chronology of the last recession of the Greenland Ice Sheet, J. Quaternary Sci., 17, 211–219, doi:10.1002/jqs.670, 2002.

Benway, H. M., Mix, A. C., Haley, B. A., and Klinkhammer, G. P.: Eastern Pacific Warm Pool paleosalinity and climate variability: 0–30 kyr, Paleoceanography, 21, PA3008, doi:10.1029/2005PA001208, 2006.

Berger, A. and Loutre, M. F.: Insolation values for the climate of the last 10 million years, Quaternary Sci. Rev., 10, 297–317, doi:10.1016/0277-3791(91)90033-Q, 1991.

Bigelow, N. H.: Climate change and Arctic ecosystems: 1. Vegetation changes north of 55degree N between the last glacial maximum, mid-Holocene, and present, J. Geophys. Res., 108, 8170, doi:10.1029/2002JD002558, 2003.

Bondeau, A., Smith, P. C., Zaehle, S., Schaphoff, S., Lucht, W., Cramer, W., Gerten, D., Lotze-Campen, H., Müller, C., Reichstein, M., and Smith, B.: Modelling the role of agriculture for the 20th century global terrestrial carbon balance, Glob. Change Biol., 13, 679–706, doi:10.1111/j.1365-2486.2006.01305.x, 2007.

Braconnot, P., Otto-Bliesner, B., Harrison, S., Joussaume, S., Peterchmitt, J.-Y., Abe-Ouchi, A., Crucifix, M., Driesschaert, E., Fichefet, Th., Hewitt, C. D., Kageyama, M., Kitoh, A., Laîné, A., Loutre, M.-F., Marti, O., Merkel, U., Ramstein, G., Valdes, P., Weber, S. L., Yu, Y., and Zhao, Y.: Results of PMIP2 coupled simulations of the Mid-Holocene and Last Glacial Maximum – Part 1: experiments and large-scale features, Clim. Past, 3, 261–277, doi:10.5194/cp-3-261-2007, 2007a.

Braconnot, P., Otto-Bliesner, B., Harrison, S., Joussaume, S., Peterchmitt, J.-Y., Abe-Ouchi, A., Crucifix, M., Driesschaert, E., Fichefet, Th., Hewitt, C. D., Kageyama, M., Kitoh, A., Loutre, M.-F., Marti, O., Merkel, U., Ramstein, G., Valdes, P., Weber, L., Yu, Y., and Zhao, Y.: Results of PMIP2 coupled simulations of the Mid-Holocene and Last Glacial Maximum – Part 2: feedbacks with emphasis on the location of the ITCZ and mid- and high latitudes heat budget, Clim. Past, 3, 279–296, doi:10.5194/cp-3-279-2007, 2007b.

Braconnot, P., Harrison, S. P., Kageyama, M., Bartlein, P. J., Masson-Delmotte, V., Abe-Ouchi, A., Otto-Bliesner, B., and Zhao, Y.: Evaluation of climate models using palaeoclimatic data, Nat. Clim. Change, 2, 417–424, doi:10.1038/nclimate1456, 2012.

Broccoli, A. J. and Manabe, S.: The influence of continental ice, atmospheric CO_2, and land albedo on the climate of the last glacial maximum, Clim. Dynam., 1, 87–99, doi:10.1007/BF01054478, 1987.

Broccoli, A. J., Dahl, K. A., and Stouffer, R. J.: Response of the ITCZ to Northern Hemisphere cooling, Geophys. Res. Lett., 33, L01702, doi:10.1029/2005GL024546, 2006.

Bromwich, D., Toracinta, E., Wei, H., Oglesby, R., Fastook, J. L., and Hughes, T. J.: Polar MM5 simulations of the winter climate of the Laurentide Ice Sheet at the LGM, J. Climate, 17, 3415–3433, 2004.

Burke, A., Marchal, O., Bradtmiller, L. I., McManus, J. F., and François, R.: Application of an inverse method to interpret 231 Pa/230 Th observations from marine sediments, Paleoceanography, 26, PA1212, doi:10.1029/2010PA002022, 2011.

Caissie, B. E., Brigham-Grette, J., Lawrence, K. T., Herbert, T. D., and Cook, M. S.: Last Glacial Maximum to Holocene sea surface conditions at Umnak Plateau, Bering Sea, as

CPD
9, 3239–3306, 2013

Assessing the impact of Laurentide Ice-Sheet topography on glacial climate

D. J. Ullman et al.

inferred from diatom, alkenone, and stable isotope records, Paleoceanography, 25, PA1206, doi:10.1029/2008PA001671, 2010.
Carlson, A. E. and Clark, P. U.: Ice sheet sources of sea level rise and freshwater discharge during the last deglaciation, Rev. Geophys., 50, RG4007, doi:10.1029/2011RG000371, 2012.
Carlson, A. E. and Winsor, K.: Northern Hemisphere ice-sheet responses to past climate warming, Nat. Geosci., 5, 607–613, doi:10.1038/ngeo1528, 2012.
Carlson, A. E., LeGrande, A. N., Oppo, D. W., Came, R. E., Schmidt, G. A., Anslow, F. S., Licciardi, J. M., and Obbink, E. A.: Rapid early Holocene deglaciation of the Laurentide ice sheet, Nat. Geosci., 1, 620–624, doi:10.1038/ngeo285, 2008a.
Carlson, A. E., Oppo, D. W., Came, R. E., LeGrande, A. N., Keigwin, L. D., and Curry, W. B.: Subtropical Atlantic salinity variability and Atlantic meridional circulation during the last deglaciation, Geology, 36, 991, doi:10.1130/G25080A.1, 2008b.
Charbit, S., Ritz, C., and Ramstein, G.: Simulations of Northern Hemisphere ice-sheet retreat: sensitivity to physical mechanisms involved during the Last Deglaciation, Quaternary Sci. Rev., 21, 243–265, 2002.
Chen, M.-T., Lin, X. P., Chang, Y.-P., Chen, Y.-C., Lo, L., Shen, C.-C., Yokoyama, Y., Oppo, D. W., Thompson, W. G., and Zhang, R.: Dynamic millennial-scale climate changes in the northwestern Pacific over the past 40 000 years, Geophys. Res. Lett., 37, L23603, doi:10.1029/2010GL045202, 2010.
Cheng, H., Zhang, P. Z., Spötl, C., Edwards, R. L., Cai, Y. J., Zhang, D. Z., Sang, W. C., Tan, M., and An, Z. S.: The climatic cyclicity in semiarid-arid central Asia over the past 500 000 years, Geophys. Res. Lett., 39, L01705, doi:10.1029/2011GL050202, 2012.
Chiang, J. C. H., Biasutti, M., and Battisti, D. S.: Sensitivity of the Atlantic Intertropical Convergence Zone to Last Glacial Maximum boundary conditions, Paleoceanography, 18, 1094, doi:10.1029/2003PA000916, 2003.
Chikamoto, M. O., Menviel, L., Abe-Ouchi, A., Ohgaito, R., Timmermann, A., Okazaki, Y., Harada, N., Oka, A., and Mouchet, A.: Variability in North Pacific intermediate and deep water ventilation during Heinrich events in two coupled climate models, Deep-Sea Res. Pt. II, 61–64, 114–126, doi:10.1016/j.dsr2.2011.12.002, 2012.
Chylek, P. and Lohmann, U.: Aerosol radiative forcing and climate sensitivity deduced from the Last Glacial Maximum to Holocene transition, Geophys. Res. Lett., 35, L04804, doi:10.1029/2007GL032759, 2008.

CPD
9, 3239–3306, 2013

Assessing the impact of Laurentide Ice-Sheet topography on glacial climate

D. J. Ullman et al.

Title Page
Abstract | Introduction
Conclusions | References
Tables | Figures
◀◀ | ▶▶
◀ | ▶
Back | Close
Full Screen / Esc
Printer-friendly Version
Interactive Discussion

Claquin, T., Roelandt, C., Kohfeld, K., Harrison, S., Tegen, I., Prentice, I. C., and Balkanski, Y.: Radiative forcing of climate by ice-age atmospheric dust, Clim. Dynam., 20, 193–202, doi:10.1007/s00382-002-0269-1, 2003.
Clark, P. U.: Surface form of the southern Laurentide Ice Sheet and its implications to ice-sheet dynamics, Geol. Soc. Am. Bull., 104, 595–605, doi:10.1130/0016-7606(1992)104<0595:SFOTSL>2.3.CO;2, 1992.
Clark, P. U.: Unstable behavior of the Laurentide ice sheet over deforming sediment and its implications for climate change, Quaternary Res., 41, 19–25, doi:10.1006/qres.1994.1002, 1994.
Clark, P. U. and Mix, A. C.: Ice sheets and sea level of the Last Glacial Maximum, Quaternary Sci. Rev., 21, 1–7, doi:10.1016/S0277-3791(01)00118-4, 2002.
Clark, P. U. and Pollard, D.: Origin of the Middle Pleistocene Transition by ice sheet erosion of regolith, Paleoceanography, 13, 1–9, doi:10.1029/97PA02660, 1998.
Clark, P. U., Licciardi, J., MacAyeal, D., and Jenson, J.: Numerical reconstruction of a soft-bedded Laurentide Ice Sheet during the last glacial maximum, Geology, 24, 679–682, doi:10.1130/0091-7613(1996)024<0679:NROASB>2.3.CO;2, 1996.
Clark, P. U., Alley, R. B., and Pollard, D.: Northern Hemisphere Ice-Sheet Influences on Global Climate Change, Science, 286, 1104–1111, doi:10.1126/science.286.5442.1104, 1999.
Clark, P. U., Dyke, A. S., Shakun, J. D., Carlson, A. E., Clark, J., Wohlfarth, B., Mitrovica, J. X., Hostetler, S. W., and McCabe, A. M.: The Last Glacial Maximum, Science, 325, 710–714, doi:10.1126/science.1172873, 2009.
Clarke, G. K. C.: Fast glacier flow: Ice streams, surging, and tidewater glaciers, J. Geophys. Res., 92, 8835–8841, doi:10.1029/JB092iB09p08835, 1987.
Climate: Long-Range Investigation, Mapping, and P. P. M. (CLIMAP): Seasonal Reconstructions of the Earth's Surface at the Last Glacial Maximum, Geological Society of America, Map and Chart Series, MC-36, 1–18, 1981.
Cook, K. H. and Held, I. M.: Stationary waves of the Ice Age climate, J. Climate, 1, 807–819, doi:10.1175/1520-0442(1988)001<0807:SWOTIA>2.0.CO;2, 1988.
Crucifix, M.: Does the Last Glacial Maximum constrain climate sensitivity?, Geophys. Res. Lett., 33, L18701, doi:10.1029/2006GL027137, 2006.
Cruz, F. W., Burns, S. J., Karmann, I., Sharp, W. D., Vuille, M., Cardoso, A. O., Ferrari, J. A., Dias, P. L. S., and Viana, O.: Insolation-driven changes in atmospheric circulation over

CPD
9, 3239–3306, 2013

the past 116 000 years in subtropical Brazil, Nature, 434, 63–66, doi:10.1038/nature03365, 2005.
Cuffey, K. M. and Clow, G. D.: Temperature, accumulation, and ice sheet elevation in central Greenland through the last deglacial transition, J. Geophys. Res., 102, 26383, doi:10.1029/96JC03981, 1997.
Cuffey, K. M., Clow, G. D., Alley, R. B., Stuiver, M., Waddington, E. D., and Saltus, R. W.: Large Arctic Temperature Change at the Wisconsin-Holocene Glacial Transition, Science, 270, 455–458, doi:10.1126/science.270.5235.455, 1995.
Curry, W. B. and Oppo, D. W.: Glacial water mass geometry and the distribution of $\delta^{13}C$ of ΣCO_2 in the western Atlantic Ocean, Paleoceanography, 20, PA1017, doi:10.1029/2004PA001021, 2005.
Dansgaard, W., Johnsen, S. J., Clausen, H. B., Dahl-Jensen, D., Gundestrup, N. S., Hammer, C. U., Hvidberg, C. S., Steffensen, J. P., Sveinbjörnsdottir, A. E., Jouzel, J., and Bond, G.: Evidence for general instability of past climate from a 250-kyr ice-core record, Nature, 364, 218–220, doi:10.1038/364218a0, 1993.
de Vernal, A. and Hillaire-Marcel, C.: Sea-ice cover, sea-surface salinity and halo-/thermocline structure of the northwest North Atlantic: modern versus full glacial conditions, Quaternary Sci. Rev., 19, 65–85, doi:10.1016/S0277-3791(99)00055-4, 2000.
de Vernal, A. and Hillaire-Marcel, C.: Natural variability of Greenland climate, vegetation, and ice volume during the past million years, Science, 320, 1622–1625, doi:10.1126/science.1153929, 2008.
de Vernal, A., Hillaire-Marcel, C., Turon, J.-L., and Matthiessen, J.: Reconstruction of sea-surface temperature, salinity, and sea-ice cover in the northern North Atlantic during the last glacial maximum based on dinocyst assemblages, Can. J. Earth Sci., 37, 725–750, 2000.
Denton, G. H. and Hughes, T. J.: The Last Great Ice Sheets, John Wiley & Sons, New York, 1981.
Denton, G. H. and Hughes, T. J.: Reconstructing the Antarctic Ice Sheet at the Last Glacial Maximum, Quaternary Sci. Rev., 21, 193–202, doi:10.1016/S0277-3791(01)00090-7, 2002.
Donohoe, A. and Battisti, D. S.: Causes of Reduced North Atlantic Storm Activity in a CAM3 Simulation of the Last Glacial Maximum, J. Climate, 22, 4793–4808, doi:10.1175/2009JCLI2776.1, 2009.

Doose, H., Prahl, F. G., and Lyle, M. W.: Biomarker temperature estimates for modern and last glacial surface waters of the California Current System between 33° and 42° N, Paleoceanography, 12, 615–622, doi:10.1029/97PA00821, 1997.
Dubois, N., Kienast, M., Normandeau, C., and Herbert, T. D.: Eastern equatorial Pacific cold tongue during the Last Glacial Maximum as seen from alkenone paleothermometry, Paleoceanography, 24, PA4207, doi:10.1029/2009PA001781, 2009.
Dyke, A. S.: An outline of North American deglaciation with emphasis on central and northern Canada, in: Quaternary Glaciations – Extent and Chronology Part II: North America, Volume 2, edited by: Ehlers, J. and Gibbard, P. L., Elsevier, Amsterdam, 373–424, 2004.
Dyke, A. S. and Prest, V. K.: Late Wisconsinan and Holocene history of the Laurentide Ice Sheet, Geogr. Phys. Quatern., 41, 237, doi:10.7202/032681ar, 1987.
Dyke, A. S., Andrews, J. T., Clark, P. U., England, J. H., Miller, G. H., Shaw, J., and Veillette, J. J.: The Laurentide and Innuitian ice sheets during the Last Glacial Maximum, Quaternary Sci. Rev., 21, 9–31, doi:10.1016/S0277-3791(01)00095-6, 2002.
Dykoski, C., Edwards, R., Cheng, H., Yuan, D., Cai, Y., Zhang, M., Lin, Y., Qing, J., an, Z., and Revenaugh, J.: A high-resolution, absolute-dated Holocene and deglacial Asian monsoon record from Dongge Cave, China, Earth Planet. Sc. Lett., 233, 71–86, doi:10.1016/j.epsl.2005.01.036, 2005.
Flower, B. P., Hastings, D. W., Hill, H. W., and Quinn, T. M.: Phasing of deglacial warming and Laurentide Ice Sheet meltwater in the Gulf of Mexico, Geology, 32, 597–600, doi:10.1130/G20604.1, 2004.
Forster, P., Ramaswamy, V., Artaxo, P., Berntsen, T., Betts, R., Fahey, D. W., Haywood, J., Lean, J., Lowe, D. C., Myhre, G., Nganga, J., Prinn, R., Raga, G., Schulz, M., and Van Dorland, R.: Changes in atmospheric constituents and in radiative forcing, in: Climate Change 2007: The Physical Science Basis, Contribution of Working Group I to the Fourth Assessment Report of the Intergovernmental Panel on Climate Change, edited by: Solomon, H. L., Qin, S., Manning, D., Chen, M., Marquis, Z., Averyt, M., Tignor, K. B., and Miller, M., Cambridge University Press, Cambridge, UK and New York, NY, USA, 130–234, 2007.
Fyke, J. and Eby, M.: Comment on “Climate sensitivity estimated from temperature reconstructions of the Last Glacial Maximum”, Science, 337, 1294, doi:10.1126/science.1221371, 2012.

Gerten, D., Schaphoff, S., Haberlandt, U., Lucht, W., and Sitch, S.: Terrestrial vegetation and water balance – hydrological evaluation of a dynamic global vegetation model, J. Hydrol., 286, 249–270, doi:10.1016/j.jhydrol.2003.09.029, 2004.

Gherardi, J.-M., Labeyrie, L., Nave, S., Francois, R., McManus, J. F., and Cortijo, E.: Glacial-interglacial circulation changes inferred from 231 Pa^{-1} 230 Th sedimentary record in the North Atlantic region, Paleoceanography, 24, PA2204, doi:10.1029/2008PA001696, 2009.

Goehring, B. M., Brook, E. J., Linge, H., Raisbeck, G. M., and Yiou, F.: Beryllium-10 exposure ages of erratic boulders in southern Norway and implications for the history of the Fennoscandian Ice Sheet, Quaternary Sci. Rev., 27, 320–336, doi:10.1016/j.quascirev.2007.11.004, 2008.

Gorbarenko, S. and Southon, J.: Detailed Japan Sea paleoceanography during the last 25 kyr: constraints from AMS dating and $\delta^{18}O$ of planktonic foraminifera, Palaeogeogr. Palaeocl., 156, 177–193, 2000.

Govil, P. and Naidu, P. D.: Evaporation-precipitation changes in the eastern Arabian Sea for the last 68 ka: implications on monsoon variability, Paleoceanography, 25, PA1210, doi:10.1029/2008PA001687, 2010.

Gregoire, L. J., Payne, A. J., and Valdes, P. J.: Deglacial rapid sea level rises caused by ice-sheet saddle collapses, Nature, 487, 219–222, doi:10.1038/nature11257, 2012.

Grootes, P. M., Stuiver, M., White, J. W. C., Johnsen, S., and Jouzel, J.: Comparison of oxygen isotope records from the GISP2 and GRIP Greenland ice cores, Nature, 366, 552–554, doi:10.1038/366552a0, 1993.

Gyllencreutz, R., Mangerud, J., Svendsen, J.-I., and Lohne, Ø.: DATED – A GIS-based reconstruction and dating database of the Eurasian deglaciation, in: Applied Quaternary Research in the Central Part of Glaciated Terrain, Special Paper 46, edited by: Johansson, P. and Sarala, P., Geological Survey of Finland, 113–120, 2007.

Hansen, J., Sato, M., Kharecha, P., Beerling, D., Berner, R., Masson-Delmotte, V., Pagani, M., Raymo, M., Royer, D. L., and Zachos, J. C.: Target Atmospheric CO_2: Where should humanity aim?, Open Atmos. Sci. J., 2, 217–231, 2008.

Harada, N., Ahagon, N., Sakamoto, T., Uchida, M., Ikehara, M., and Shibata, Y.: Rapid fluctuation of alkenone temperature in the southwestern Okhotsk Sea during the past 120 ky, Global Planet. Change, 53, 29–46, doi:10.1016/j.gloplacha.2006.01.010, 2006.

Hargreaves, J. C., Annan, J. D., Yoshimori, M., and Abe-Ouchi, A.: Can the Last Glacial Maximum constrain climate sensitivity?, Geophys. Res. Lett., 39, L24702, doi:10.1029/2012GL053872, 2012.

Harrison, S. P., Yu, G., Takahara, H., and Prentice, I. C.: Palaeovegetation diversity of temperate plants in east Asia, Nature, 413, 129–130, doi:10.1038/35093166, 2001.

Hays, J. D., Imbrie, J., and Shackleton, N. J.: Variations in the Earth's orbit: pacemaker of the ice ages, Science, 194, 1121–1132, doi:10.1126/science.194.4270.1121, 1976.

He, F., Shakun, J. D., Clark, P. U., Carlson, A. E., Liu, Z., Otto-Bliesner, B. L., and Kutzbach, J. E.: Northern Hemisphere forcing of Southern Hemisphere climate during the last deglaciation, Nature, 494, 81–85, doi:10.1038/nature11822, 2013.

Headly, M. A. and Severinghaus, J. P.: A method to measure Kr/N_2 ratios in air bubbles trapped in ice cores and its application in reconstructing past mean ocean temperature, J. Geophys. Res., 112, D19105, doi:10.1029/2006JD008317, 2007.

Herbert, T. D., Schuffert, J. D., Andreasen, D., Heusser, L., Lyle, M., Mix, A. C., Ravelo, A. C., Stott, L. D., and Herguera, J. C.: Collapse of the California Current during glacial maxima linked to climate change on land, Science, 293, 71–76, doi:10.1126/science.1059209, 2001.

Herguera, J. C., Herbert, T., Kashgarian, M., and Charles, C.: Intermediate and deep water mass distribution in the Pacific during the Last Glacial Maximum inferred from oxygen and carbon stable isotopes, Quaternary Sci. Rev., 29, 1228–1245, doi:10.1016/j.quascirev.2010.02.009, 2010.

Hofer, D., Raible, C. C., Dehnert, A., and Kuhlemann, J.: The impact of different glacial boundary conditions on atmospheric dynamics and precipitation in the North Atlantic region, Clim. Past, 8, 935–949, doi:10.5194/cp-8-935-2012, 2012.

Holmgren, K., Lee-Thorp, J. A., Cooper, G. R. J., Lundblad, K., Partridge, T. C., Scott, L., Sithaldeen, R., Siep Talma, A., and Tyson, P. D.: Persistent millennial-scale climatic variability over the past 25 000 years in Southern Africa, Quaternary Sci. Rev., 22, 2311–2326, doi:10.1016/S0277-3791(03)00204-X, 2003.

Huang, S. P., Pollack, H. N., and Shen, P.-Y.: A late Quaternary climate reconstruction based on borehole heat flux data, borehole temperature data, and the instrumental record, Geophys. Res. Lett., 35, L13703, doi:10.1029/2008GL034187, 2008.

Huybers, P. and Wunsch, C.: Obliquity pacing of the late Pleistocene glacial terminations, Nature, 434, 491–494, doi:10.1038/nature03401, 2005.

Hyde, W. T. and Peltier, W. R.: Effect of altered boundary conditions on GCM studies of the climate of the Last Glacial Maximum, Geophys. Res. Lett., 20, 939–942, doi:10.1029/92GL02626, 1993.

Imbrie, J. and Imbrie, J. Z.: Modeling the climatic response to orbital variations, Science, 207, 943–953, doi:10.1126/science.207.4434.943, 1980.

IPCC: The Physical Science Basis, Contribution of Working Group I to the Fourth Assessment Report of the Intergovernmental Panel on Climate Change, edited by: Solomon, H. L., Qin, S., Manning, D., Chen, M., Marquis, Z., Averyt, M., Tignor, K. B., and Miller, M., Cambridge University Press, Cambridge, UK and New York, NY, USA, 2007.

Jackson, S. T., Webb, R. S., Anderson, K. H., Overpeck, J. T., Webb III, T., Williams, J. W., and Hansen, B. C. S.: Vegetation and environment in Eastern North America during the Last Glacial Maximum, Quaternary Sci. Rev., 19, 489–508, doi:10.1016/S0277-3791(99)00093-1, 2000.

Jahn, A., Claussen, M., Ganopolski, A., and Brovkin, V.: Quantifying the effect of vegetation dynamics on the climate of the Last Glacial Maximum, Clim. Past, 1, 1–7, doi:10.5194/cp-1-1-2005, 2005.

Jenson, J. W., MacAyeal, D. R., Clark, P. U., Ho, C. L., and Vela, J. C.: Numerical modeling of subglacial sediment deformation: implications for the behavior of the Lake Michigan Lobe, Laurentide Ice Sheet, J. Geophys. Res., 101, 8717, doi:10.1029/96JB00169, 1996.

Joos, F. and Spahni, R.: Rates of change in natural and anthropogenic radiative forcing over the past 20 000 years, P. Natl. Acad. Sci. USA, 105, 1425–1430, 2008.

Jouzel, J., Masson-Delmotte, V., Cattani, O., Dreyfus, G., Falourd, S., Hoffmann, G., Minster, B., Nouet, J., Barnola, J. M., Chappellaz, J., Fischer, H., Gallet, J. C., Johnsen, S., Leuenberger, M., Loulergue, L., Luethi, D., Oerter, H., Parrenin, F., Raisbeck, G., Raynaud, D., Schilt, A., Schwander, J., Selmo, E., Souchez, R., Spahni, R., Stauffer, B., Steffensen, J. P., Stenni, B., Stocker, T. F., Tison, J. L., Werner, M., and Wolff, E. W.: Orbital and millennial Antarctic climate variability over the past 800 000 years, Science, 317, 793–796, doi:10.1126/science.1141038, 2007.

Kageyama, M., Valdes, P. J., Ramstein, G., Hewitt, C., and Wyputta, U.: Northern Hemisphere storm tracks in present day and Last Glacial Maximum climate simulations: a comparison of the European PMIP models, J. Climate, 12, 742–760, doi:10.1175/1520-0442(1999)012<0742:NHSTIP>2.0.CO;2, 1999.

Kao, S. J., Wu, C.-R., Hsin, Y.-C., and Dai, M.: Effects of sea level change on the upstream Kuroshio Current through the Okinawa Trough, Geophys. Res. Lett., 33, L16604, doi:10.1029/2006GL026822, 2006.

Katsuki, K., Khim, B.-K., Itaki, T., Okazaki, Y., Ikehara, K., Shin, Y., Yoon, H. I., and Kang, C. Y.: Sea-ice distribution and atmospheric pressure patterns in southwestern Okhotsk Sea since the Last Glacial Maximum, Global Planet. Change, 72, 99–107, doi:10.1016/j.gloplacha.2009.12.005, 2010.

Keigwin, L. and Gorbarenko, S.: Sea level, surface salinity of the Japan Sea, and the Younger Dryas event in the northwestern Pacific Ocean, Quaternary Res., 360, 346–360, 1992.

Klinkhammer, G. P., Mix, A. C., and Haley, B. A.: Increased dissolved terrestrial input to the coastal ocean during the last deglaciation, Geochem. Geophy. Geosy., 10, Q03009, doi:10.1029/2008GC002219, 2009.

Kohn, M. J. and McKay, M.: Stable isotopes of fossil teeth corroborate key general circulation model predictions for the Last Glacial Maximum in North America, Geophys. Res. Lett., 37, L22702, doi:10.1029/2010GL045404, 2010.

Koutavas, A., Lynch-Stieglitz, J., Marchitto, T. M., and Sachs, J. P.: El Niño-like pattern in ice age tropical Pacific sea surface temperature, Science, 297, 226–230, doi:10.1126/science.1072376, 2002.

Kucera, M., Rosell-Melé, A., Schneider, R., Waelbroeck, C., and Weinelt, M.: Multiproxy approach for the reconstruction of the glacial ocean surface (MARGO), Quaternary Sci. Rev., 24, 813–819, doi:10.1016/j.quascirev.2004.07.017, 2005.

Kurek, J., Cwynar, L. C., Ager, T. A., Abbott, M. B., and Edwards, M. E.: Late Quaternary paleoclimate of western Alaska inferred from fossil chironomids and its relation to vegetation histories, Quaternary Sci. Rev., 28, 799–811, doi:10.1016/j.quascirev.2008.12.001, 2009.

Lambeck, K., Purcell, A., Zhao, J., and Svensson, N.-O.: The Scandinavian Ice Sheet: from MIS 4 to the end of the Last Glacial Maximum, Boreas, 39, 410–435, doi:10.1111/j.1502-3885.2010.00140.x, 2010.

Langen, P. L. and Vinther, B. M.: Response in atmospheric circulation and sources of Greenland precipitation to glacial boundary conditions, Clim. Dynam., 32, 1035–1054, doi:10.1007/s00382-008-0438-y, 2008.

Lea, D. W., Pak, D. K., and Spero, H. J.: Climate Impact of Late Quaternary Equatorial Pacific Sea Surface Temperature Variations, Science, 289, 1719–1724, doi:10.1126/science.289.5485.1719, 2000.

Lea, D. W., Pak, D. K., Peterson, L. C., and Hughen, K. A: Synchroneity of tropical and high-latitude Atlantic temperatures over the last glacial termination, Science, 301, 1361–1364, doi:10.1126/science.1088470, 2003.
Lea, D. W., Pak, D. K., Belanger, C. L., Spero, H. J., Hall, M. A., and Shackleton, N. J.: Paleoclimate history of Galápagos surface waters over the last 135 000 yr, Quaternary Sci. Rev., 25, 1152–1167, doi:10.1016/j.quascirev.2005.11.010, 2006.
LeGrande, A. N. and Schmidt, G. A.: Sources of Holocene variability of oxygen isotopes in paleoclimate archives, Clim. Past, 5, 441–455, doi:10.5194/cp-5-441-2009, 2009.
LeGrande, A. N., Schmidt, G. A., Shindell, D. T., Field, C. V., Miller, R. L., Koch, D. M., Faluvegi, G., and Hoffmann, G.: Consistent simulations of multiple proxy responses to an abrupt climate change event, P. Natl. Acad. Sci. USA, 103, 837–842, doi:10.1073/pnas.0510095103, 2006.
Lemieux-Dudon, B., Blayo, E., Petit, J.-R., Waelbroeck, C., Svensson, A., Ritz, C., Barnola, J.-M., Narcisi, B. M., and Parrenin, F.: Consistent dating for Antarctic and Greenland ice cores, Quaternary Sci. Rev., 29, 8–20, doi:10.1016/j.quascirev.2009.11.010, 2010.
Levitus, S. and Boyer, T.: World Ocean Atlas 1994, vol. 2: Oxygen, NOAA Atlas NESDIS 2, US Gov. Printing Office, Wash., DC, 186 pp., 1994a.
Levitus, S. and Boyer, T., World Ocean Atlas 1994, vol. 4: Temperature, NOAA Atlas NESDIS 4, US Gov. Printing Office, Wash., DC, 117 pp., 1994b.
Levitus, S., Burgett, R., and Boyer, T.: World Ocean Atlas 1994, vol. 3: Salinity, NOAA Atlas NESDIS e, US Gov. Printing Office, Wash., DC, 99 pp., 1994.
Licciardi, J. M., Clark, P. U., Jenson, J. W., and Macayeal, D. R.: Deglaciation of a soft-bedded Laurentide ice sheet, Quaternary Sci. Rev., 17, 427–448, doi:10.1016/S0277-3791(97)00044-9, 1998.
Licciardi, J. M., Teller, J. T., and Clark, P. U.: Freshwater routing by the Laurentide Ice Sheet during the last deglaciation, Geophys. Monogr.-Am. Geophys., 112, 177–202, 1999.
Lippold, J., Luo, Y., Francois, R., Allen, S. E., Gherardi, J., Pichat, S., Hickey, B., and Schulz, H.: Strength and geometry of the glacial Atlantic Meridional Overturning Circulation, Nat. Geosci., 5, 813–816, doi:10.1038/ngeo1608, 2012.
Liu, Z., Otto-Bliesner, B. L., He, F., Brady, E. C., Tomas, R., Clark, P. U., Carlson, A. E., Lynch-Stieglitz, J., Curry, W., Brook, E., Erickson, D., Jacob, R., Kutzbach, J., and Cheng, J.: Transient simulation of last deglaciation with a new mechanism for Bolling–Allerod warming, Science, 325, 310–314, doi:10.1126/science.1171041, 2009.

Lohmann, U. and Feichter, J.: Global indirect aerosol effects: a review, Atmos. Chem. Phys., 5, 715–737, doi:10.5194/acp-5-715-2005, 2005.
Lüthi, D., Le Floch, M., Bereiter, B., Blunier, T., Barnola, J.-M., Siegenthaler, U., Raynaud, D., Jouzel, J., Fischer, H., Kawamura, K., and Stocker, T. F.: High-resolution carbon dioxide concentration record 650 000–800 000 years before present, Nature, 453, 379–382, doi:10.1038/nature06949, 2008.
Lynch-Stieglitz, J., Adkins, J. F., Curry, W. B., Dokken, T., Hall, I. R., Herguera, J. C., Hirschi, J. J.-M., Ivanova, E. V., Kissel, C., Marchal, O., Marchitto, T. M., McCave, I. N., McManus, J. F., Mulitza, S., Ninnemann, U., Peeters, F., Yu, E.-F., and Zahn, R.: Atlantic meridional overturning circulation during the Last Glacial Maximum, Science, 316, 66–69, doi:10.1126/science.1137127, 2007.
Mahowald, N., Kohfeld, K., Hansson, M., Balkanski, Y., Harrison, S. P., Prentice, I. C., Schulz, M., and Rodhe, H.: Dust sources and deposition during the last glacial maximum and current climate: a comparison of model results with paleodata from ice cores and marine sediments, J. Geophys. Res., 104, 15895, doi:10.1029/1999JD900084, 1999.
Manabe, S. and Broccoli, A. J.: The influence of continental ice sheets on the climate of an ice age, J. Geophys. Res., 90, 2167–2190, doi:10.1029/JD090iD01p02167, 1985.
Mangelsdorf, K., Güntner, U., and Rullkötter, J.: Climatic and oceanographic variations on the California continental margin during the last 160 kyr, Org. Geochem., 31, 829–846, doi:10.1016/S0146-6380(00)00066-8, 2000.
Marshall, S. J. and Clark, P. U.: Basal temperature evolution of North American ice sheets and implications for the 100-kyr cycle, Geophys. Res. Lett., 29, 2214, doi:10.1029/2002GL015192, 2002.
Marshall, S. J., Tarasov, L., Clarke, G. K. C., and Peltier, W. R.: Glaciological reconstruction of the Laurentide Ice Sheet: physical processes and modelling challenges, Can. J. Earth Sci., 37, 769–793, doi:10.1139/cjes-37-5-769, 2000.
Matsumoto, K., Oba, T., Lynch-Stieglitz, J., and Yamamoto, H.: Interior hydrography and circulation of the glacial Pacific Ocean, Quaternary Sci. Rev., 21, 1693–1704, doi:10.1016/S0277-3791(01)00142-1, 2002.
McManus, J. F., Francois, R., Gherardi, J.-M., Keigwin, L. D., and Brown-Leger, S.: Collapse and rapid resumption of Atlantic meridional circulation linked to deglacial climate changes, Nature, 428, 834–837, doi:10.1038/nature02494, 2004.

Melles, M., Brigham-Grette, J., Glushkova, O. Y., Minyuk, P. S., Nowaczyk, N. R., and Hubberten, H.-W.: Sedimentary geochemistry of core PG1351 from Lake El'gygytgyn – a sensitive record of climate variability in the East Siberian Arctic during the past three glacial–interglacial cycles, J. Paleolimnol., 37, 89–104, doi:10.1007/s10933-006-9025-6, 2007.

Melles, M., Brigham-Grette, J., Minyuk, P. S., Nowaczyk, N. R., Wennrich, V., DeConto, R. M., Anderson, P. M., Andreev, A. A., Coletti, A., Cook, T. L., Haltia-Hovi, E., Kukkonen, M., Lozhkin, A. V., Rosén, P., Tarasov, P., Vogel, H., and Wagner, B.: 2.8 million years of Arctic climate change from Lake El'gygytgyn, NE Russia, Science, 337, 315–320, doi:10.1126/science.1222135, 2012.

Mix, A. C., Morey, A. E., Pisias, N. G., and Hostetler, S. W.: Foraminiferal faunal estimates of paleotemperature: circumventing the no-analog problem yields cool Ice Age tropics, Paleoceanography, 14, 350–359, doi:10.1029/1999PA900012, 1999.

Mix, A. C., Bard, E., and Schneider, R.: Environmental processes of the ice age: land, oceans, glaciers (EPILOG), Quaternary Sci. Rev., 20, 627–657, doi:10.1016/S0277-3791(00)00145-1, 2001.

Mohtadi, M., Lückge, A., Steinke, S., Groeneveld, J., Hebbeln, D., and Westphal, N.: Late Pleistocene surface and thermocline conditions of the eastern tropical Indian Ocean, Quaternary Sci. Rev., 29, 887–896, doi:10.1016/j.quascirev.2009.12.006, 2010.

Monnin, E., Indermühle, A., Dällenbach, A., Flückiger, J., Stauffer, B., Stocker, T. F., Raynaud, D., and Barnola, J. M.: Atmospheric CO_2 concentrations over the last glacial termination, Science, 291, 112–114, doi:10.1126/science.291.5501.112, 2001.

Monnin, E., Steig, E. J., Siegenthaler, U., Kawamura, K., Schwander, J., Stauffer, B., Stocker, T. F., Morse, D. L., Barnola, J.-M., Bellier, B., Raynaud, D., and Fischer, H.: Evidence for substantial accumulation rate variability in Antarctica during the Holocene, through synchronization of CO_2 in the Taylor Dome, Dome C and DML ice cores, Earth Planet. Sc. Lett., 224, 45–54, doi:10.1016/j.epsl.2004.05.007, 2004.

Oerlemans, J.: The role of ice sheets in the Pleistocene climate, Norsk Geol. Tidsskr., 71, 155–161, 1991.

Oppo, D. W. and Sun, Y.: Amplitude and timing of sea-surface temperature change in the northern South China Sea: dynamic link to the East Asian monsoon, Geology, 33, 785–788, doi:10.1130/G21867.1, 2005.

Ortiz, J., Mix, A., Hostetler, S., and Kashgarian, M.: The California Current of the Last Glacial Maximum: reconstruction at 42° N based on multiple proxies, Paleoceanography, 12, 191–205, doi:10.1029/96PA03165, 1997.
Otto-Bliesner, B. L., Brady, E. C., Clauzet, G., Tomas, R., Levis, S., and Kothavala, Z.: Last Glacial Maximum and Holocene Climate in CCSM3, J. Climate, CCSM3, 2526–2544, doi:10.1175/JCLI3748.1, 2006.
Otto-Bliesner, B. L., Hewitt, C. D., Marchitto, T. M., Brady, E., Abe-Ouchi, A., Crucifix, M., Murakami, S., and Weber, S. L.: Last Glacial Maximum ocean thermohaline circulation: PMIP2 model intercomparisons and data constraints, Geophys. Res. Lett., 34, L12706, doi:10.1029/2007GL029475, 2007.
Pahnke, K., Zahn, R., Elderfield, H., and Schulz, M.: 340 000-year centennial-scale marine record of Southern Hemisphere climatic oscillation, Science, 301, 948–952, doi:10.1126/science.1084451, 2003.
PALAEOSENS Project Members: Making sense of palaeoclimate sensitivity, Nature, 491, 683–691, doi:10.1038/nature11574, 2012.
Partin, J. W., Cobb, K. M., Adkins, J. F., Clark, B., and Fernandez, D. P.: Millennial-scale trends in west Pacific warm pool hydrology since the Last Glacial Maximum, Nature, 449, 452–455, doi:10.1038/nature06164, 2007.
Pausata, F. S. R., Li, C., Wettstein, J. J., Kageyama, M., and Nisancioglu, K. H.: The key role of topography in altering North Atlantic atmospheric circulation during the last glacial period, Clim. Past, 7, 1089–1101, doi:10.5194/cp-7-1089-2011, 2011.
Payne, A. J.: Limit cycles in the basal thermal regime of ice sheets, J. Geophys. Res., 100, 4249, doi:10.1029/94JB02778, 1995.
Peltier, W. R.: Ice age paleotopography, Science, 265, 195–201, doi:10.1126/science.265.5169.195, 1994.
Peltier, W. R.: Global glacial isostasy and the surface of the Ice-Age Earth: the ICE-5G (VM2) model and GRACE, Annu. Rev. Earth Pl. Sc., 32, 111–149, doi:10.1146/annurev.earth.32.082503.144359, 2004.
Peltier, W. R.: Closure of the budget of global sea level rise over the GRACE era: the importance and magnitudes of the required corrections for global glacial isostatic adjustment, Quaternary Sci. Rev., 28, 1658–1674, doi:10.1016/j.quascirev.2009.04.004, 2009.
Peltier, W. R.: Closing the budget of global sea level rise: The GRACE correction for GIA over the oceans, in: Workshop Report of the Intergovernmental Panel of Climate Change Work-

CPD
9, 3239–3306, 2013

Assessing the impact of Laurentide Ice-Sheet topography on glacial climate

D. J. Ullman et al.

shop on Sea Level Rise and Ice Sheet Instabilities, edited by: Stocker, T. F., Qin, D., Plattner, G.-K., Tignor, M., Allen, S., and Midgley, P. M., IPCC Working Group Technical Support Unit, University of Bern, Bern, Switzerland, 157–159, 2010.

Peltier, W. R. and Drummond, R.: Rheological stratification of the lithosphere: a direct inference based upon the geodetically observed pattern of the glacial isostatic adjustment of the North American continent, Geophys. Res. Lett., 35, L16314, doi:10.1029/2008GL034586, 2008.

Penner, J. E., Dong, X., and Chen, Y.: Observational evidence of a change in radiative forcing due to the indirect aerosol effect, Nature, 427, 231–234, doi:10.1038/nature02234, 2004.

Peterse, F., Prins, M. A., Beets, C. J., Troelstra, S. R., Zheng, H., Gu, Z., Schouten, S., and Damsté, J. S. S.: Decoupled warming and monsoon precipitation in East Asia over the last deglaciation, Earth Planet. Sc. Lett., 301, 256–264, doi:10.1016/j.epsl.2010.11.010, 2011.

Peterson, L. C.: Rapid Changes in the Hydrologic Cycle of the Tropical Atlantic During the Last Glacial, Science, 290, 1947–1951, doi:10.1126/science.290.5498.1947, 2000.

Petit, J.-R., Briat, M., and Royer, A.: Ice age aerosol content from East Antarctic ice core samples and past wind strength, Nature, 293, 391–394, doi:10.1038/293391a0, 1981.

Pickett, E. J., Harrison, S. P., Hope, G., Harle, K., Dodson, J. R., Kershaw, P. A., Prentice, C. I., Backhouse, J., Colhoun, E. A., D'Costa, D., Flenley, J., Grindrod, J., Haberle, S., Hassell, C., Kenyon, C., Macphail, M., Martin, H., Martin, A. H., McKenzie, M., Newsome, J. C., Penny, D., Powell, J., Raine, J. I., Southern, W., Stevenson, J., Sutra, J.-P., Thomas, I., van der Kaars, S., and Ward., J.: Pollen-based reconstructions of biome distributions for Australia, Southeast Asia and the Pacific (SEAPAC region) at 0, 6000 and 18 000 ^{14}C yr BP, J. Biogeogr., 31, 1381–1444, doi:10.1111/j.1365-2699.2004.01001.x, 2004.

Pollard, D. and PMIP Participating Groups: Comparisons of ice-sheet surface mass budgets from Paleoclimate Modeling Intercomparison Project (PMIP) simulations, Global Planet. Change, 24, 79–106, doi:10.1016/S0921-8181(99)00071-5, 2000.

Power, M. J., Marlon, J., Ortiz, N., Bartlein, P. J., Harrison, S. P., Mayle, F. E., Ballouche, A., Bradshaw, R. H. W., Carcaillet, C., Cordova, C., Mooney, S., Moreno, P., Prentice, I. C., Thonicke, K., Tinner, W., Whitlock, C., Zhang, Y., Zhao, Y., Anderson, R. S., Beer, R., Behling, H., Briles, C., Brown, K. J., Brilunelle, A., Bush, M., Camill, P., Chu, G. Q., Clark, J., Colombaroli, D., Daniels, M., Dodson, J., Doughty, E., Edwards, M. E., Fisinger, W., Foster, D., Gaillard, M.-J., Gavin, D. G., Gobet, E., Haberle, S., Hallett, D. J., Higuera, P., Hope, G., Horn, S., Inoue, J., Kaltenrieder, P., Kennedy, L., Kong, Z. C., Larsen, C., Long, C. J., Lunch, J., Lunch, B., McGlone, M., Meeks, S., Mensing, S., Meyer, G., Minckley, T., Mohr, J., Newnham, R.,

CPD
9, 3239–3306, 2013

Assessing the impact of Laurentide Ice-Sheet topography on glacial climate

D. J. Ullman et al.

Noti, R., Oswald, W., Pierce, J., Richard, P. J. H., Shuman, B. J., Takahara, H., Toney, J., Turney, C., Umbanhower, C., Vandergoes, M., Vanniere, B., Vescovi, E., Walsh, M., Wang, X., Williams, N., Wilmshurst, J., and Zhang, J. H.: Changes in fire regimes since the Last Glacial Maximum: an assessment based on a global synthesis and analysis of charcoal data, Clim. Dynam., 30, 887–907, doi:10.1007/s00382-007-0334-x, 2007.

Prentice, I. C. and Jolly, D.: Mid-Holocene and glacial-maximum vegetation geography of the northern continents and Africa, J. Biogeogr., 27, 507–519, doi:10.1046/j.1365-2699.2000.00425.x, 2000.

Ray, N. and Adams, J. M.: A GIS-based Vegetation Map of the World at the Last Glacial Maximum (25 000–15 000 BP), Internet Archaeol., 11, 1–44, 2001.

Reader, M. C., Fung, I., and McFarlane, N.: The mineral dust aerosol cycle during the Last Glacial Maximum, J. Geophys. Res., 104, 9381–9398, doi:10.1029/1999JD900033, 1999.

Ritz, S. P., Stocker, T. F., Grimalt, J. O., Menviel, L., and Timmermann, A.: Estimated strength of the Atlantic overturning circulation during the last deglaciation, Nat. Geosci., 6, 208–212, doi:10.1038/ngeo1723, 2013.

Rosell-Melé, A., Bard, E., Emeis, K.-C., Grieger, B., Hewitt, C., Müller, P. J., and Schneider, R. R.: Sea surface temperature anomalies in the oceans at the LGM estimated from the alkenone-U 37 K$'$ index: comparison with GCMs, Geophys. Res. Lett., 31, L03208, doi:10.1029/2003GL018151, 2004.

Ruddiman, W. F.: Earth's Climate?: Past and Future, W. H. Freeman, New York, 2001.

Russell, G. L., Miller, J. R., Rind, D., Ruedy, R. A., Schmidt, G. A., and Sheth, S.: Comparison of model and observed regional temperature changes during the past 40 years, J. Geophys. Res., 105, 14891, doi:10.1029/2000JD900156, 2000.

Šafanda, J. and Rajver, D.: Signature of the last ice age in the present subsurface temperatures in the Czech Republic and Slovenia, Global Planet. Change, 29, 241–257, doi:10.1016/S0921-8181(01)00093-5, 2001.

Sagawa, T., Toyoda, K., and Oba, T.: Sea surface temperature record off central Japan since the Last Glacial Maximum using planktonic foraminiferal Mg Ca^{-1} thermometry, J. Quaternary Sci., 21, 63–73, doi:10.1002/jqs.941, 2006.

Sarnthein, M., Pflaumann, U., and Weinelt, M.: Past extent of sea ice in the northern North Atlantic inferred from foraminiferal paleotemperature estimates, Paleoceanography, 18, 1047, doi:10.1029/2002PA000771, 2003.

CPD
9, 3239–3306, 2013

Assessing the impact of Laurentide Ice-Sheet topography on glacial climate

D. J. Ullman et al.

Title Page
Abstract | Introduction
Conclusions | References
Tables | Figures
◀◀ | ▶▶
◀ | ▶
Back | Close
Full Screen / Esc
Printer-friendly Version
Interactive Discussion

Sawada, K. and Handa, N.: Variability of the path of the Kuroshio ocean current over the past 25 000 years, 392, 592–595, doi:10.1038/33391, 1998.
Schmidt, G. A., Annan, J. D., Bartlein, P. J., Cook, B. I., Guilyardi, E., Hargreaves, J. C., Harrison, S. P., Kageyama, M., LeGrande, A. N., Konecky, B., Lovejoy, S., Mann, M. E., Masson-Delmotte, V., Risi, C., Thompson, D., Timmermann, A., Tremblay, L.-B., and Yiou, P.: Using paleo-climate comparisons to constrain future projections in CMIP5, Clim. Past Discuss., 9, 775–835, doi:10.5194/cpd-9-775-2013, 2013.
Schmittner, A., Urban, N. M., Shakun, J. D., Mahowald, N. M., Clark, P. U., Bartlein, P. J., Mix, A. C., and Rosell-Melé, A.: Climate sensitivity estimated from temperature reconstructions of the Last Glacial Maximum, Science, 334, 1385–1388, doi:10.1126/science.1203513, 2011.
Schmittner, A., Urban, N. M., Shakun, J. D., Mahowald, N. M., Clark, P. U., Bartlein, P. J., Mix, A. C., and Rosell-Melé, A.: Response to Comment on "Climate Sensitivity Estimated from Temperature Reconstructions of the Last Glacial Maximum", Science, 337, 1294–1294, doi:10.1126/science.1221634, 2012.
Seki, O., Kawamura, K., Ikehara, M., Nakatsuka, T., and Oba, T.: Variation of alkenone sea surface temperature in the Sea of Okhotsk over the last 85 kyrs, Org. Geochem., 35, 347–354, doi:10.1016/j.orggeochem.2003.10.011, 2004.
Seki, O., Nakatsuka, T., Kawamura, K., Saitoh, S.-I., and Wakatsuchi, M.: Time-series sediment trap record of alkenones from the western Sea of Okhotsk, Mar. Chem., 104, 253–265, doi:10.1016/j.marchem.2006.12.002, 2007.
Shakun, J. D. and Carlson, A. E.: A global perspective on Last Glacial Maximum to Holocene climate change, Quaternary Sci. Rev., 29, 1801–1816, doi:10.1016/j.quascirev.2010.03.016, 2010.
Shakun, J. D., Clark, P. U., He, F., Marcott, S. A., Mix, A. C., Liu, Z., Otto-Bliesner, B., Schmittner, A., and Bard, E.: Global warming preceded by increasing carbon dioxide concentrations during the last deglaciation, Nature, 484, 49–54, doi:10.1038/nature10915, 2012.
Shiga, K. and Koizumi, I.: Latest Quaternary oceanographic changes in the Okhotsk Sea based on diatom records, Mar. Micropaleontol., 38, 91–117, 1999.
Sitch, S., Smith, B., Prentice, I. C., Arneth, A., Bondeau, A., Cramer, W., Kaplan, J. O., Levis, S., Lucht, W., Sykes, M. T., Thonicke, K., and Venevsky, S.: Evaluation of ecosystem dynamics, plant geography and terrestrial carbon cycling in the LPJ dynamic global vegetation model, Global Change Biol., 9, 161–185, doi:10.1046/j.1365-2486.2003.00569.x, 2003.

CPD
9, 3239–3306, 2013

Skinner, L. C. and Shackleton, N. J.: Rapid transient changes in northeast Atlantic deep water ventilation age across Termination I, Paleoceanography, 19, PA2005, doi:10.1029/2003PA000983, 2004.

Steinke, S., Chiu, H.-Y., Yu, P.-S., Shen, C.-C., Erlenkeuser, H., Löwemark, L., and Chen, M.-T.: On the influence of sea level and monsoon climate on the southern South China Sea freshwater budget over the last 22 000 years, Quaternary Sci. Rev., 25, 1475–1488, doi:10.1016/j.quascirev.2005.12.008, 2006.

Steinke, S., Kienast, M., Groeneveld, J., Lin, L.-C., Chen, M.-T., and Rendle-Bühring, R.: Proxy dependence of the temporal pattern of deglacial warming in the tropical South China Sea: toward resolving seasonality, Quaternary Sci. Rev., 27, 688–700, doi:10.1016/j.quascirev.2007.12.003, 2008.

Steinke, S., Glatz, C., Mohtadi, M., Groeneveld, J., Li, Q., and Jian, Z.: Past dynamics of the East Asian monsoon: No inverse behaviour between the summer and winter monsoon during the Holocene, Global Planet. Change, 78, 170–177, doi:10.1016/j.gloplacha.2011.06.006, 2011.

Stott, L., Timmermann, A., and Thunell, R.: Southern Hemisphere and deep-sea warming led deglacial atmospheric CO_2 rise and tropical warming, Science, 318, 435–438, doi:10.1126/science.1143791, 2007.

Sun, Y., Oppo, D. W., Xiang, R., Liu, W., and Gao, S.: Last deglaciation in the Okinawa Trough: Subtropical northwest Pacific link to Northern Hemisphere and tropical climate, Paleoceanography, 20, PA4005, doi:10.1029/2004PA001061, 2005.

Svensson, A., Andersen, K. K., Bigler, M., Clausen, H. B., Dahl-Jensen, D., Davies, S. M., Johnsen, S. J., Muscheler, R., Parrenin, F., Rasmussen, S. O., Röthlisberger, R., Seierstad, I., Steffensen, J. P., and Vinther, B. M.: A 60 000 year Greenland stratigraphic ice core chronology, Clim. Past, 4, 47–57, doi:10.5194/cp-4-47-2008, 2008.

Tada, R., Irino, T., and Koizumi, I.: Land-ocean linkages over orbital and millennial timescales recorded in Late Quaternary sediments of the Japan Sea, Paleoceanography, 14, 236–247, doi:10.1029/1998PA900016, 1999.

Tarasov, L. and Peltier, W. R.: A geophysically constrained large ensemble analysis of the deglacial history of the North American ice-sheet complex, Quaternary Sci. Rev., 23, 359–388, doi:10.1016/j.quascirev.2003.08.004, 2004.

Tharammal, T., Paul, A., Merkel, U., and Noone, D.: Influence of Last Glacial Maximum boundary conditions on the global water isotope distribution in an atmospheric general circulation model, Clim. Past, 9, 789–809, doi:10.5194/cp-9-789-2013, 2013.

Thompson, L. G., Mosley-Thompson, E., Davis, M. E., Lin, P. N., Henderson, K. A., Cole-Dai, J., Bolzan, J. F., and Liu, K. B.: Late glacial stage and Holocene tropical ice core records from Huascaran, Peru, Science, 269, 46–50, doi:10.1126/science.269.5220.46, 1995.

Thompson, L. G., Davis, M. E., Mosley-Thompson, E., Sowers, T. A., Henderson, K. A., Zagorodnov, V. S., Lin, P.-N., Mikhalenko, V. N., Campen, R. K., Bolzan, J. F., Cole-Dai, J., and Francou, B.: A 25 000-year tropical climate history from Bolivian ice cores, Science, 282, 1858–1864, doi:10.1126/science.282.5395.1858, 1998.

Thompson, L. G., Mosley-Thompson, E., and Henderson, K. A.: Ice-core palaeoclimate records in tropical South America since the last glacial maximum, J. Quaternary Sci., 15, 377–394, 2000.

Timm, O. and Timmermann, A.: Simulation of the last 21 000 years using accelerated transient boundary conditions, J. Climate, 20, 4377–4401, doi:10.1175/JCLI4237.1, 2007.

Toscano, M. A., Peltier, W. R., and Drummond, R.: ICE-5G and ICE-6G models of post-glacial relative sea-level history applied to the Holocene coral reef record of northeastern St Croix, U.S.V.I.: investigating the influence of rotational feedback on GIA processes at tropical latitudes, Quaternary Sci. Rev., 30, 3032–3042, doi:10.1016/j.quascirev.2011.07.018, 2011.

Viau, A. E., Gajewski, K., Sawada, M. C., and Bunbury, J.: Low- and high-frequency climate variability in eastern Beringia during the past 25 000 years, Can. J. Earth Sci., 45, 1435–1453, doi:10.1139/E08-036, 2008.

Visser, K., Thunell, R., and Stott, L.: Magnitude and timing of temperature change in the Indo–Pacific warm pool during deglaciation, Nature, 421, 152–155, doi:10.1038/nature01297, 2003.

Waelbroeck, C., Paul, A., Kucera, M., Rosell-Melé, A., Weinelt, M., Schneider, R., Mix, A. C., Abelmann, A., Armand, L., Bard, E., Barker, S., Barrows, T. T., Benway, H., Cacho, I., Chen, M.-T., Cortijo, E., Crosta, X., de Vernal, A., Dokken, T., Duprat, J., Elderfield, H., Eynaud, F., Gersonde, R., Hayes, A., Henry, M., Hillaire-Marcel, C., Huang, C.-C., Jansen, E., Juggins, S., Kallel, N., Kiefer, T., Kienast, M., Labeyrie, L., Leclaire, H., Londeix, L., Mangin, S., Matthiessen, J., Marret, F., Meland, M., Morey, A. E., Mulitza, S., Pflaumann, U., Pisias, N. G., Radi., T., Rochon, A., Rohling, E. J., Sbaffi, L., Schäfer-Neth, C., Solignac, S., Spero, H., Tachikawa, K., and Turon, J.-L.: Constraints on the magnitude and patterns of

CPD
9, 3239–3306, 2013

Assessing the impact of Laurentide Ice-Sheet topography on glacial climate

D. J. Ullman et al.

ocean cooling at the Last Glacial Maximum, Nat. Geosci., 2, 127–132, doi:10.1038/ngeo411, 2009.
Wang, Y. J., Cheng, H., Edwards, R. L., An, Z. S., Wu, J. Y., Shen, C. C., and Dorale, J. A.: A high-resolution absolute-dated late Pleistocene Monsoon record from Hulu Cave, China, Science, 294, 2345–2348, doi:10.1126/science.1064618, 2001.
Wang, X., Auler, A. S., Edwards, R. L., Cheng, H., Cristalli, P. S., Smart, P. L., Richards, D. A., and Shen, C.-C.: Wet periods in northeastern Brazil over the past 210 kyr linked to distant climate anomalies, Nature, 432, 740–743, doi:10.1038/nature03067, 2004.
Wang, X., Auler, A. S., Edwards, R. L., Cheng, H., Ito, E., Wang, Y., Kong, X., and Solheid, M.: Millennial-scale precipitation changes in southern Brazil over the past 90 000 years, Geophys. Res. Lett., 34, L23701, doi:10.1029/2007GL031149, 2007.
Weber, S. L., Drijfhout, S. S., Abe-Ouchi, A., Crucifix, M., Eby, M., Ganopolski, A., Murakami, S., Otto-Bliesner, B., and Peltier, W. R.: The modern and glacial overturning circulation in the Atlantic ocean in PMIP coupled model simulations, Clim. Past, 3, 51–64, doi:10.5194/cp-3-51-2007, 2007.
Weldeab, S., Schneider, R. R., Kölling, M., and Wefer, G.: Holocene African droughts relate to eastern equatorial Atlantic cooling, Geology, 33, 981–984, doi:10.1130/G21874.1, 2005.
Weldeab, S., Schneider, R. R., and Kölling, M.: Deglacial sea surface temperature and salinity increase in the western tropical Atlantic in synchrony with high latitude climate instabilities, Earth Planet. Sc. Lett., 241, 699–706, doi:10.1016/j.epsl.2005.11.012, 2006.
Weldeab, S., Lea, D. W., Schneider, R. R., and Andersen, N.: 155 000 years of West African monsoon and ocean thermal evolution, Science, 316, 1303–1307, doi:10.1126/science.1140461, 2007.
Williams, J. W.: Variations in tree cover in North America since the last glacial maximum, Global Planet. Change, 35, 1–23, 2003.
Williams, J. W., Tarasov, P., Brewer, S., and Notaro, M.: Late Quaternary variations in tree cover at the northern forest-tundra ecotone, J. Geophys. Res., 116, G01017, doi:10.1029/2010JG001458, 2011.
Williams, P. W., King, D. N. T., Zhao, J.-X., and Collerson, K. D.: Late Pleistocene to Holocene composite speleothem ^{18}O and ^{13}C chronologies from South Island, New Zealand – did a global Younger Dryas really exist?, Earth Planet. Sc. Lett., 230, 301–317, 2005.
Wunsch, C.: Determining paleoceanographic circulations, with emphasis on the Last Glacial Maximum, Quaternary Sci. Rev., 22, 371–385, doi:10.1016/S0277-3791(02)00177-4, 2003.

CPD
9, 3239–3306, 2013

Title Page
Abstract Introduction
Conclusions References
Tables Figures
◂◂ ▸▸
◂ ▸
Back Close
Full Screen / Esc
Printer-friendly Version
Interactive Discussion

Xu, J., Holbourn, A., Kuhnt, W., Jian, Z., and Kawamura, H.: Changes in the thermocline structure of the Indonesian outflow during Terminations I and II, Earth Planet. Sc. Lett., 273, 152–162, doi:10.1016/j.epsl.2008.06.029, 2008.

Yamamoto, M., Suemune, R., and Oba, T.: Equatorward shift of the subarctic boundary in the northwestern Pacific during the last deglaciation, Geophys. Res. Lett., 32, L05609, doi:10.1029/2004GL021903, 2005.

Yu, E.-F., Francois, R., and Bacon, M. P.: Similar rates of modern and last-glacial ocean thermohaline circulation inferred from radiochemical data, Nature, 379, 689–694, doi:10.1038/379689a0, 1996.

Ziegler, M., Nürnberg, D., Karas, C., Tiedemann, R., and Lourens, L. J.: Persistent summer expansion of the Atlantic Warm Pool during glacial abrupt cold events, Nat. Geosci., 1, 601–605, doi:10.1038/ngeo277, 2008.

CPD
9, 3239–3306, 2013

Assessing the impact of Laurentide Ice-Sheet topography on glacial climate

D. J. Ullman et al.

Table 1. Boundary conditions for experiments presented in this paper. The abbreviations for the orbital parameters refer to eccentricity (E), obliquity in degree (O), and angular precession (longitude of perihelion, or omega) in degree (P) (Berger and Loutre, 1991).

Simulation	Time Slice	Orbital Parameters	Greenhouse Gas Concentrations	Sea level Change	LIS geometry and Max Elevation
21 ka-L	21 ka	E: 0.019398 O: 22.989 P: 113.98	CO_2: 188 ppm CH_4: 385 ppm N_2O: 200 ppm	−120 m	Licciardi et al. (1998) 3560 m
21 ka-5G	21 ka	E: 0.019398 O: 22.989 P: 113.98	CO_2: 188 ppm CH_4: 385 ppm N_2O: 200 ppm	−120 m	Peltier (2004) 4520 m
14 ka-L	14 ka	E: 0.020180 O: 24.004 P: 228.37	CO_2: 239 ppm CH_4: 630 ppm N_2O: 261 ppm	−86 m	Licciardi et al. (1998) 2890 m
14 ka-5G	14 ka	E: 0.020180 O: 24.004 P: 228.37	CO_2: 239 ppm CH_4: 630 ppm N_2O: 261 ppm	−86 m	Peltier (2004) 3400 m
Control	Preindustrial (0 ka)	E: 0.017236 O: 23.446 P: 101.37	CO_2: 285 ppm CH_4: 791 ppm N_2O: 275 ppm	0 m	Modern

CPD
9, 3239–3306, 2013

Assessing the impact of Laurentide Ice-Sheet topography on glacial climate

D. J. Ullman et al.

Title Page
Abstract | Introduction
Conclusions | References
Tables | Figures
◀ | ▶
Back | Close
Full Screen / Esc
Printer-friendly Version
Interactive Discussion

Table 2. δ^{18}O proxy records used in model-data comparison of δ^{18}Oa and δ^{18}Oo. Records were selected that have continuous coverage from the LGM to preindustrial. For ocean records, an additional selection criteria required the existence an associated independent temperature proxy (i.e., Mg/Ca) to calculate $\delta^{18}O_{seawater}$ from $\delta^{18}O_{calcite}$ (Bemis et al., 1998).

Reference	Proxy	Lat (° N)	Lon (° E)
	δ^{18}Oa records		
Bar-Matthews et al. (2003)	Speleothem	31.5	35.0
Cheng et al. (2012)	Speleothem	42.9	81.8
Cruz et al. (2005)	Speleothem	−27.2	−49.2
Dykoskie et al. (2005)	Speleothem	−27.2	−49.2
Holmgren et al. (2003)	Speleothem	−24.0	29.2
Partin et al. (2007)	Speleothem	4.0	114.0
Wang et al. (2001)	Speleothem	25.3	108.1
Wang et al. (2007)	Speleothem	−27.2	−49.2
Williams et al. (2005)	Speleothem	−42.0	172.0
Dansgaard et al. (1993)	GRIP ice core	72.6	−37.6
Grootes et al. (1993)	GISP2 ice core	72.6	−38.5
Svensson et al. (2008)	NGRIP ice core	75.1	−42.3
Thompson et al. (1998)	Bolivia ice core	−18.0	−69.0
Kohn and McKay (2010)	Megafauna teeth (LGM only)	45.0	−108.0
	δ^{18}Oo records		
Benway et al. (2006)	Marine sediment core	7.9	−83.6
Carlson et al. (2008b)	Marine sediment core	33.7	−57.6
Carlson et al. (2008b)	Marine sediment core	32.8	−76.3
Carlson et al. (2008b)	Marine sediment core	−27.5	−46.5
Chen et al. (2010)	Marine sediment core	26.6	125.8
Govil and Naidu (2010)	Marine sediment core	14.5	72.7
Klinkhammer et al. (2009)	Marine sediment core	7.9	83.6
Koutavas et al. (2002)	Marine sediment core	−1.2	−89.7
Lea et al. (2000)	Marine sediment core	2.3	−91.0
Lea et al. (2003)	Marine sediment core	10.7	−64.9
Lea et al. (2006)	Marine sediment core	0.5	−92.4
Mohtadi et al. (2010)	Marine sediment core	−1.5	100.1
Mohtadi et al. (2010)	Marine sediment core	−5.9	103.2
Oppo and Sun (2005)	Marine sediment core	19.6	117.6
Pahnke et al. (2003)	Marine sediment core	−45.5	174.9
Sagawa et al. (2006)	Marine sediment core	36.1	141.8
Skinner and Shackleton (2004)	Marine sediment core	37.8	−10.2
Steinke et al. (2006)	Marine sediment core	6.6	113.4
Steinke et al. (2008)	Marine sediment core	6.6	113.4
Steinke et al. (2011)	Marine sediment core	19.5	116.3
Stott et al. (2007)	Marine sediment core	−10.6	125.4
Stott et al. (2007)	Marine sediment core	−5.0	133.4
Stott et al. (2007)	Marine sediment core	6.3	125.8
Visser et al. (2003)	Marine sediment core	−4.7	117.9
Weldeab et al. (2005)	Marine sediment core	2.5	9.4
Weldeab et al. (2006)	Marine sediment core	−4.6	−36.6
Weldeab et al. (2007)	Marine sediment core	2.5	9.4
Ziegler et al. (2008)	Marine sediment core	29.0	−87.1
Xu et al. (2008)	Marine sediment core	−13.1	121.8

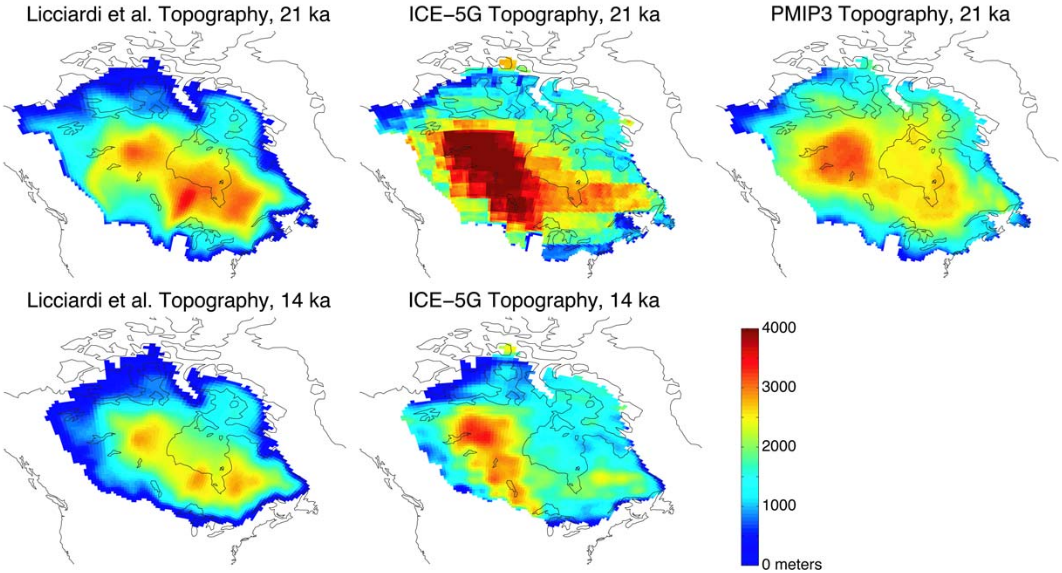

Fig. 1. Laurentide Ice Sheet topographies used in 21 ka (top row) and 14 ka (bottom row) simulations. The left column presents the Licciardi et al. (1998) reconstructions used in 21 ka-L and 14 ka-L. The middle column presents the ICE-5G reconstructions (Peltier, 2004) used in 21 ka-5G and 14 ka-5G. For comparison, the single plot in the right column shows the LIS topography used in the PMIP3 boundary conditions (http://pmip3.lsce.ipsl.fr/).

CPD
9, 3239–3306, 2013

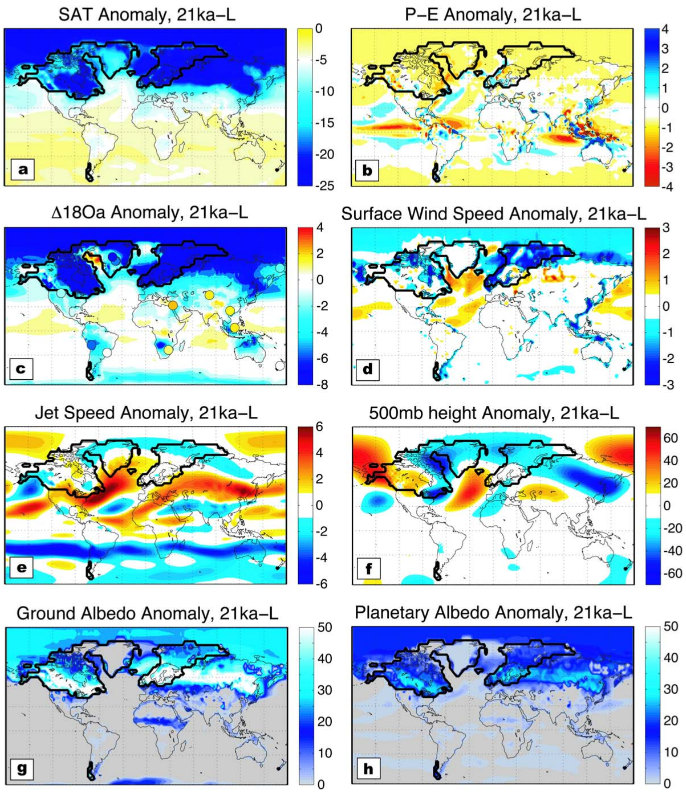

Fig. 2. 21 ka anomalies (21 ka-L minus 0 ka), for the following annually averaged atmospheric variables: **(a)** Surface Air Temperature (°C); **(b)** Precipiation minus Evaporation (mm day^{-1}); **(c)** δ^{18}Oa (‰) with anomalies from proxy records (see Table A1) plotted as circles with the same colorbar; **(d)** Surface Wind Speed (m s^{-1}); **(e)** Atmospheric Jet Speed (m s^{-1}); **(f)** Geopotential height at the 500 mb level, with zonal mean removed (m); **(g)** Ground Albedo (%); **(h)** Planetary Albedo (%). Ice sheet extents outlined in bold black line.

CPD
9, 3239–3306, 2013

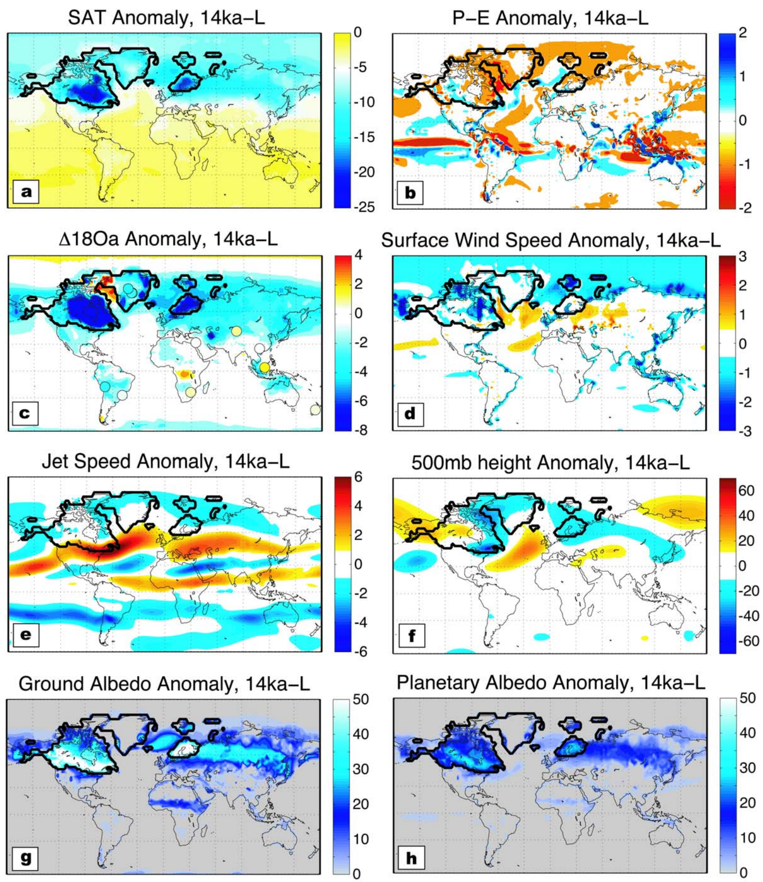

Fig. 3. Same as Fig. 2, but for 14 ka anomalies (14 ka-L minus 0 ka).

CPD
9, 3239–3306, 2013

Assessing the impact of Laurentide Ice-Sheet topography on glacial climate

D. J. Ullman et al.

Title Page
Abstract Introduction
Conclusions References
Tables Figures
◀I ▶I
◀ ▶
Back Close
Full Screen / Esc
Printer-friendly Version
Interactive Discussion

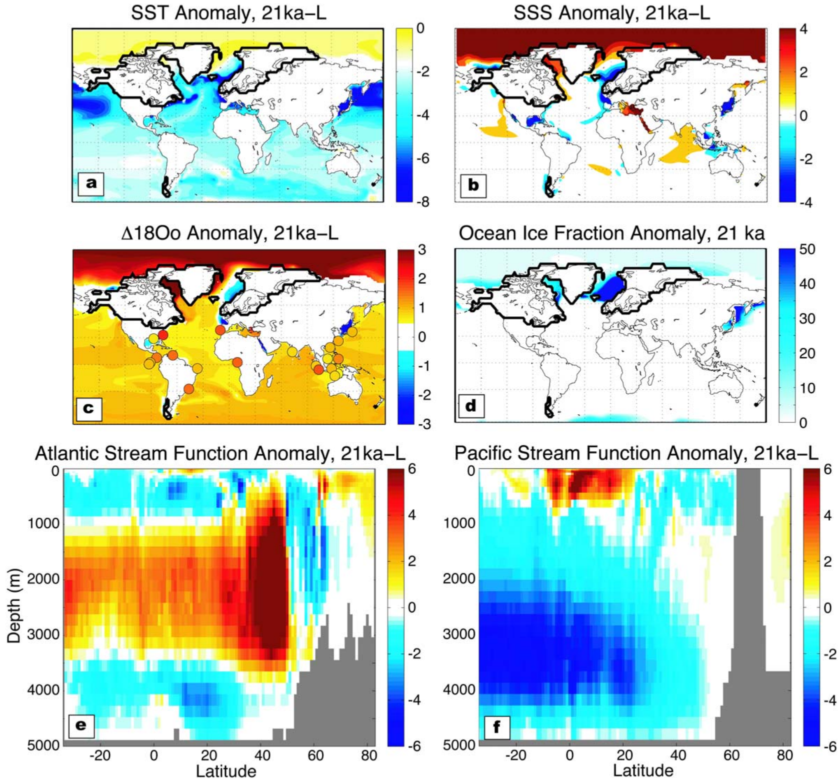

Fig. 4. 21 ka anomalies (21 ka-L minus 0 ka), for the following annually averaged ocean variables variables: **(a)** Sea Surface Temperature (˚C); **(b)** Sea Surface Salinity (psu); **(c)** δ^{18}Oo (‰) with anomalies from proxy records (see Table A1) plotted as circles with the same colorbar; **(d)** Sea Ice Fraction (%); **(e)** Atlantic Ocean overturning stream function (Sv); **(f)** Pacific Ocean overturning stream function (Sv).

CPD
9, 3239–3306, 2013

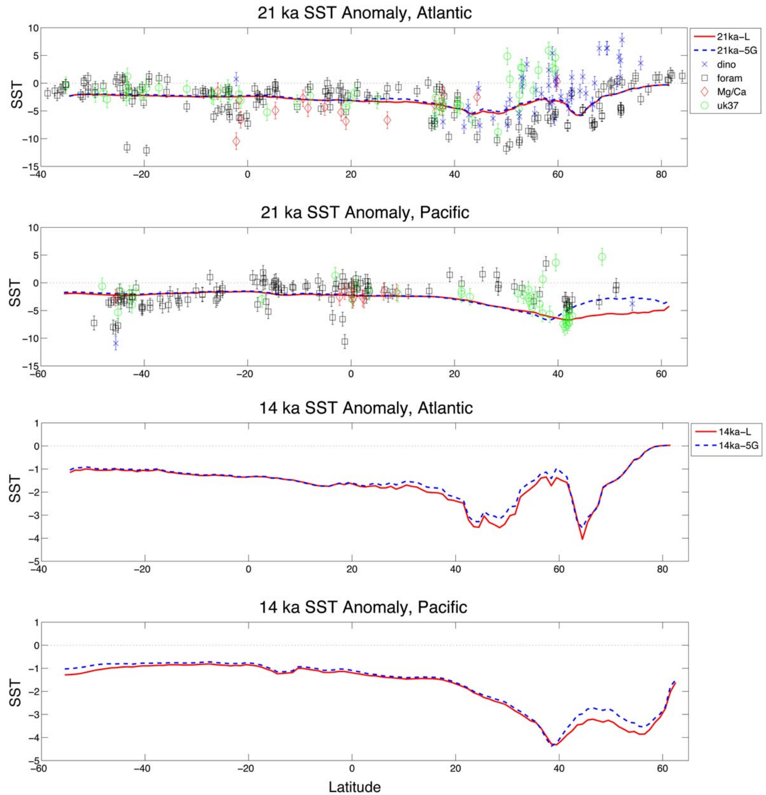

Fig. 5. Longitudinal transects of SST anomalies averaged across the Atlantic and Pacific basins, with comparison to published MARGO data and uncertainties for the 21 ka simulations (Waelbroeck et al., 2009). MARGO data is separated by categories of proxies used in the reconstruction of SST as follows: blue x's, dinoflagellates; black squares, foraminifera; red diamonds, Mg/Ca; and green circles, alkenones (U^K_{37}). A similar compilation of SST records does not exist for 14 ka.

CPD
9, 3239–3306, 2013

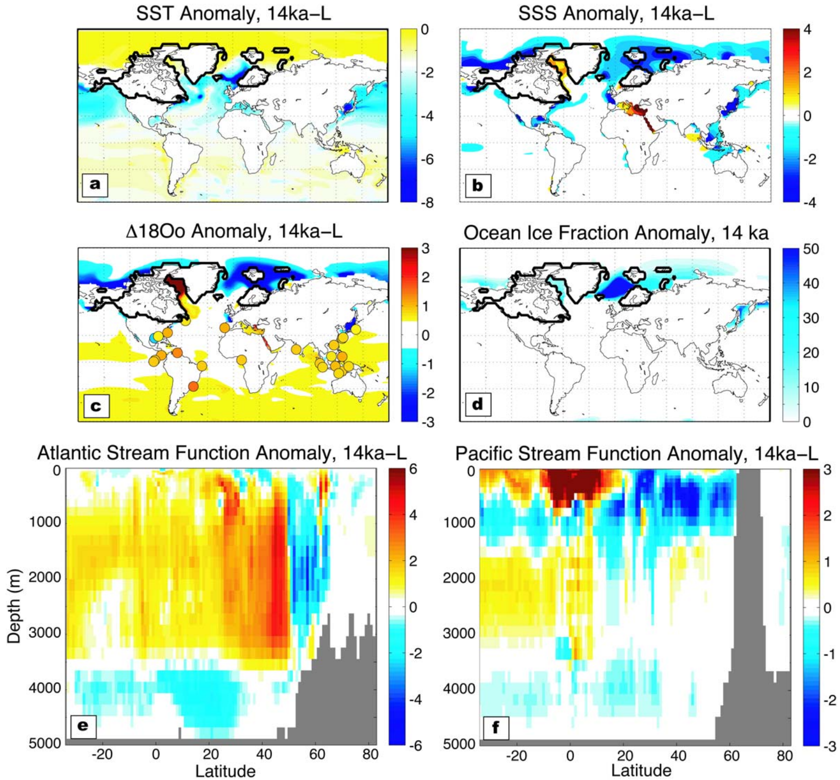

Fig. 6. Same as Fig. 4, but for 14 ka anomalies (14 ka-L minus 0 ka).

CPD
9, 3239–3306, 2013

Assessing the impact of Laurentide Ice-Sheet topography on glacial climate

D. J. Ullman et al.

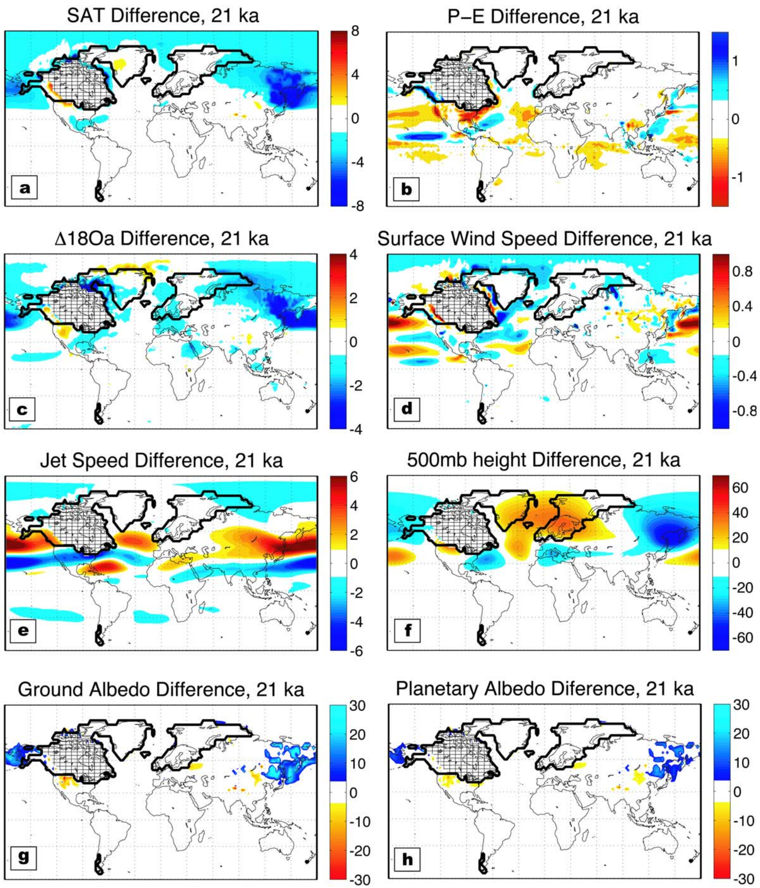

Fig. 7. Differences between 21 ka simulations (21 ka-L minus 21 ka-5G) for the same atmospheric variables presented in Fig. 2. The LIS is masked out to focus on downstream differences.

CPD
9, 3239–3306, 2013

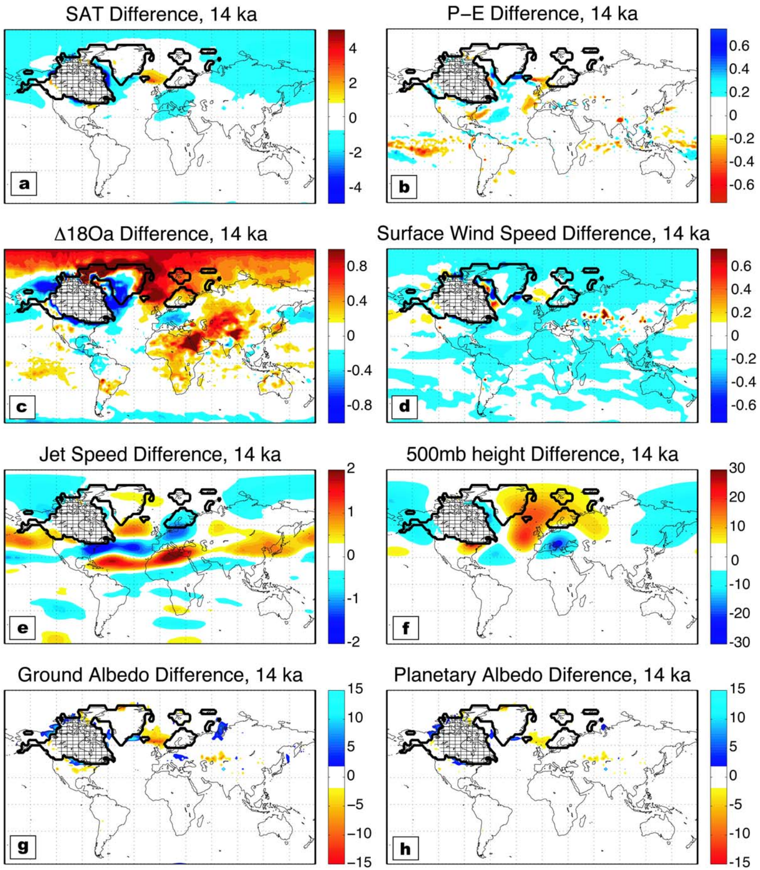

Fig. 8. Same as Fig. 7, but with the atmospheric differences between 14 ka simulations (14 ka-L minus 14 ka-5G).

CPD
9, 3239–3306, 2013

Assessing the impact of Laurentide Ice-Sheet topography on glacial climate

D. J. Ullman et al.

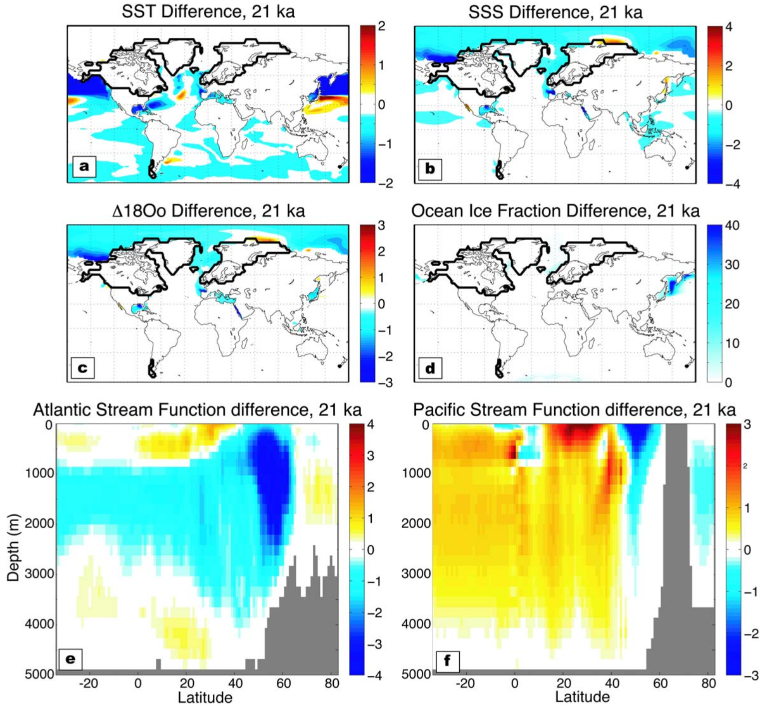

Fig. 9. Differences between 21 ka simulations (21 ka-L minus 21 ka-5G) for the same ocean variables presented in Fig. 4.

CPD
9, 3239–3306, 2013

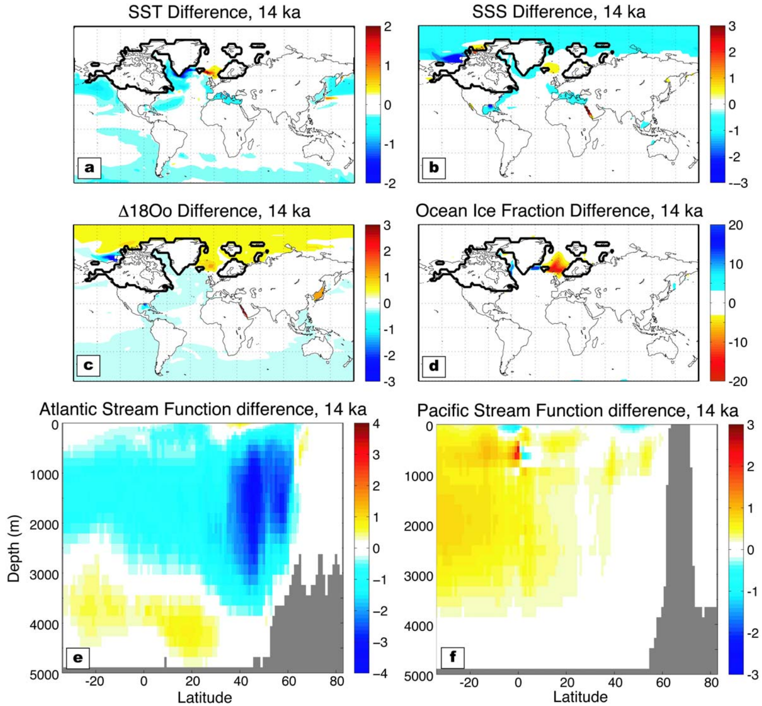

Fig. 10. Same as Fig. 9, but with the ocean differences between 14 ka simulations (14 ka-L minus 14 ka-5G).